*J. Fluid Mech.* (1983), *vol.* 134, *pp.* 357–399
*Printed in Great Britain*



# Gravity currents moving along a lateral boundary in a rotating fluid

By R. W. GRIFFITHS† AND E. J. HOPFINGER
Institut de Mécanique de Grenoble, B.P. 53 X, Centre de Tri, 38041 Grenoble, France

(Received 4 January 1983 and in revised form 10 May 1983)

Density currents in a rotating fluid are produced by releasing a volume of buoyant fluid from a lock at one end of a long rotating channel. Coriolis forces hold the current against one wall. It is observed that the velocity and depth of the nose decrease exponentially in time, implying that the nose can effectively come to a halt at a finite distance from the lock. In reality though, the flow regime eventually changes and a viscous wedge-shaped intrusion continues. The high-Reynolds-number currents contain three-dimensional turbulence a short distance behind the nose, but the influence of rotation causes this to become quasi-two-dimensional further upstream. The intrusion and turbulent motions represent a forcing to the lower layer that produces vortex and wave-like motions which penetrate deep into the lower-layer fluid. It is shown that the exponential decay can be attributed to radiation of momentum by these inertial waves.

The width $l$ of the turbulent current varies with distance behind the nose, from 0.6 times the local time-dependent deformation radius at the 'head' to $l \approx R_0$ far upstream, where $R_0$ is the initial deformation radius in the lock. The nose of the boundary current is unstable, with billows appearing near the tip of the intruding nose and leading to an intermittent breakup of the 'head' structure and oscillations of the nose velocity. These oscillations are rapid, often having frequencies much greater than $f$ (where $f = 2\Omega$ is the Coriolis parameter), and, along with the production of the turbulence that is so characteristic of the currents, are attributed to a Kelvin–Helmholtz instability. Rotationally dominated baroclinic waves appear only a very large distance behind the nose.

## 1. Introduction

When buoyant fluid is released in a rotating system near a vertical wall, Coriolis forces constrain the density-driven flow to be along the wall. The importance of side boundaries in removing the constraints of rotation upon the spreading of fluid as it collapses under gravity, and the consequent formation of a coastal jet, appears to have been first discussed by Gill (1976). In this vein, Wadhams, Linden & Gill (1979) proposed that the presence of the east coast of Greenland caused less-dense water from the surface of the Norwegian Sea to flow south as the East Greenland current. Such boundary currents are an important feature in coastal oceanography, and several aspects of them have recently been studied.

In experiments with a two-layer density-driven flow that initially formed an axisymmetric current around a vertical cylindrical wall, Griffiths & Linden (1981,

† Present address: Research School of Earth Sciences, The Australian National University, P.O. Box 4, Canberra 2600, Australia.

1982) investigated the stability of such a boundary current to rotationally dominated† waves and qualitatively described the way in which instability leads to a broader current containing rotationally dominated turbulence. A theoretical treatment of the linear stability problem is difficult if the influence of the sharp front at the edge of the boundary current is to be included, though Killworth & Stern (1982) discussed a hydrostatic model in which only one layer of fluid is dynamically active. Stern (1980) also developed a similarity solution to the inviscid long-wave equations describing a laminar current allowing only slow variation of width or velocity along the wall and flow over a very deep and passive ambient layer, and discussed the nonlinear stability of this solution. He suggested that, for the unsteady case in which a current is preceded by an intruding nose, the solution might be valid far upstream of (behind) the intruding nose. Though only valid in the limit of slow streamwise variations, the solution would then indicate that the nose of an intruding layer could either steepen into an internal bore, for which the fluid velocity behind the nose is greater than the velocity of the nose, or form into an ever thinning wedge shape that would be limited only by viscous effects. The similarity solution was extended to the case with two layers of finite depth and arbitrary potential vorticities by Stern, Whitehead & Hua (1982) and predicts the velocity profile and width far upstream of the nose in terms of the depth $h_u$ (far upstream) at the wall. With the assumption that the flow near the wall is steady and energy conserving there follows the result that the current width is always in the range 0.41–0.52 times the deformation radius $(g'h_u)^{\frac{1}{2}}/f$, where $g' = g\Delta\rho/\rho$ is the reduced gravity and $f = 2\Omega$ is the Coriolis parameter. More significantly though, Stern *et al.* find that the width $l$ of a steady laminar current should satisfy the inequality

$$l \leqslant \frac{u_N}{2f} < \frac{1}{\sqrt{2}} \frac{(g'h_u)^{\frac{1}{2}}}{f},$$

where $u_N$ is the propagation velocity of the nose, irrespective of the amount of dissipation or mixing.

Observations of the propagation of an intruding nose produced by a slow continuous supply of buoyant fluid from a confined source on a wall (Stern 1980; Griffiths & Linden 1981) indicated that the bore solution was realized and that rotationally dominated instabilities, possibly related to those predicted by Stern, appeared at the nose and along the trailing flow. The flow remained laminar, but only small Reynolds numbers ($< 10^2$) were studied. More interesting in the geophysical context are experiments reported by Stern *et al.* (1982), which prompted the work described in this paper. High Reynolds numbers and more-controlled initial conditions were achieved by releasing a fixed volume of buoyant fluid, possessing uniform potential vorticity, from a lock at one end of a straight channel. Without rotation the resulting flow would correspond to surface gravity currents of the type described for instance in the review by Simpson (1982). When the system is rotating, however, Coriolis forces hold the current against one wall, producing a three-dimensional flow and altering interfacial mixing. For Reynolds numbers of order $10^3$ and greater, the outer edge of the current was reported to be turbulent, and hence definition of a characteristic, dynamically significant width for comparison with the similarity solution was somewhat ambiguous. Stern *et al.* chose to measure the distance from the wall to a line of maximum shear, inside which the flow was supposed to be quasisteady, laminar and unidirectional. They found this width to be $0.42(g'h_u)^{\frac{1}{2}}/f$,

† The term 'rotationally dominated' is used here to describe flow perturbations for which the Rossby number is small, but does not restrict attention to geostrophic flow.

in excellent agreement with that predicted (although the measured width was larger when the ratio of current width to depth was less that a value of order unity). They also noticed that the velocity of the nose decreased with time and in some experiments the nose even came to rest. It was suggested that this stagnation of the nose might be due to a blocking effect of an unstable wave.

More-detailed observations and measurements of the structure and dynamics of similar gravity currents with high Reynolds numbers are reported here. A qualitative description of the principal features of the flow is given in §3. The flow in a short region near the nose (discussed in §4), though itself strongly influenced by the background rotation, develops billows whose wavelength, maximum amplitude and growth rate all indicate that they are the result of a Kelvin–Helmholtz instability that is little influenced by rotation. The instability is therefore similar to that which occurs on non-rotating gravity currents and is not the result of rotationally dominated, hydrostatic instabilities discussed by Stern (1980). The nose velocity is found to decrease as the nose moves along the channel, as was noticed by Stern *et al.*, but we demonstrate in §4 that this decrease is exponential in time. The velocity decay-time scales with the rotation rate $\Omega$ and a global Froude number based on lock parameters. The billows and three-dimensional turbulence produced in both fluids near the nose are constantly left behind by the propagating nose to form a more slowly moving turbulent current in which the eddy motions become quasi-two-dimensional under the influence of the background rotation. Measurements of the profiles of mean streamwise velocity at locations upstream of the nose are discussed in §5 and permit us to compare the total width of the turbulent current (revealed by dye) to the width defined on the basis of maximum velocity or maximum shear. In §6 we describe observations of vortex and wavelike motions induced in the deep lower layer by the passage of the boundary current, and in §7 we develop arguments that support the idea that the exponential decay of the nose velocity is a consequence of momentum loss by inertial wave radiation. This important aspect is further supported by the behaviour of a current running over a shallow layer, as presented in §8. The results are summarized in §9, which also contain further remarks on vortex formation beneath the current and on the growth of rotationally dominated waves far upstream.

## 2. Realization of the 'dambreak' experiments

The density currents described here were produced by removing a vertical barrier that initially retained a volume of fresh water which lay at one end of a channel and floated on a much larger volume of dilute salt solution. The channel was 200 cm long, 30 cm wide and was carefully levelled about the vertical axis of rotation of a direct-drive turntable. For most experiments the total depth $D$ of fluid in the channel was 50 cm ($\pm 1$ cm). However, in a small number of experiments $D = 10$ cm was used.

The fresh water that was destined to form the gravity current was contained in one of the three different lock geometries shown in figure 1. The different geometries, while being strongly constrained by practicalities in the laboratory, were designed to give different volumes of fresh water and different ratios of lock width to lock length. Lock A has a horizontal area $A_0 = 600$ cm, B of 500 cm$^2$ and C of 150 cm$^2$, while A and B have width-to-length ratios of $\frac{3}{2}$ and $\frac{1}{5}$ respectively. Depths of the fresh water covered the range $3 \leqslant H_0 \leqslant 12$ cm and the removable barrier (0.2 cm thick) extended 10–15 cm below the surface. The density difference between the layers was found by measuring the specific gravity of each fluid to 0.0002 with a hydrometer, the difference in density being 0.2–1.5 % of that of fresh water $\rho_0$ with an uncertainty

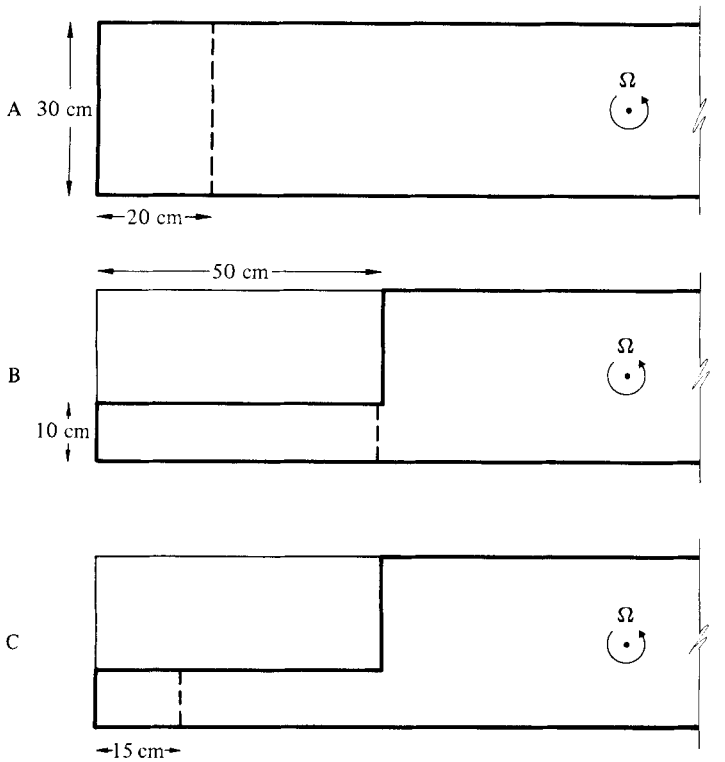


FIGURE 1. The three lock geometries in plan. In each case the barrier (broken line) extends 15 cm below the free surface. Direction of rotation is anticlockwise.

of $\pm 0.05\%$ of $\rho_0$. Thus the reduced gravity $g' = g\Delta\rho/\rho_0$ lay in the range $2 \leqslant g' \leqslant 15$ cm s$^{-2}$. The direction of rotation was always anticlockwise so that the current always lay against the right-hand wall of the channel when looking in the direction of propagation.

The experiments were performed as follows. Once the deep layer of salt solution had spun up to the desired rotation rate ($0.1 \leqslant f \leqslant 2.1$ rad s$^{-1}$), fresh water was slowly placed on the free surface inside the lock using a porous-foam float. Very little mixing occurred during filling. Both fluids had been left to approach room temperature, and their temperatures differed by less than 0.1 °C. When the fresh water reached the desired depth $H_0$ the filling mechanism was removed and the system left (for about one hour) to return to solid-body rotation. It was found that a covering lid was unnecessary as any motions induced by evaporative convection and surface wind stress were not detectable in long-time-exposure photographs of particle motions, and were therefore less than $\frac{1}{40}$ of the speed of the nose.

Once the two-layer system was in solid-body rotation the barrier was smoothly withdrawn, leaving the dyed fresh water to spread along the free surface. At approximately the same time an electronic timing system was started. This triggered one or more cameras at a preset accurate time interval so that we obtained a regular sequence of photographs of the flow. For some experiments two cameras were mounted on a moving counter-balanced carriage in such a way that one photographed the flow from above and the other recorded it from the side, simultaneously. These gave clear close-up views with little distortion. In other runs, an inclined mirror was

placed alongside the channel, and a single camera mounted in the rotating frame far above the turntable recorded both plan and side views of the full length of the gravity current. The flow was made visible by adding food dye, fluorescent dye or neutrally buoyant polystyrene particles to the fluid before beginning the experiment. The particles were illuminated by a horizontal sheet of light 2–3 cm thick and positioned at selected depths. Time-exposure photographs of particles were designed to reveal, in particular, motions in the deep lower layer.

All measurements were taken from the photographs: the nose position was obtained from both side and plan views and the current width and depth on the wall (also as functions of time) were taken at several positions behind the nose. The depths and widths measured here were simply those indicated by the visible dye. These were well-defined quantities everywhere, although the presence of convolutions on the outer edge of the flow and on the density interface at the wall made mean measurements in a short region just behind the nose unreliable and ambiguous. Mixing across the density interface in this same region accentuated the difficulty of measuring the depth of the flow. Independent measurements of the current width and structure upstream of the nose were obtained in a number of runs by injecting neutrally buoyant dye into the flow from an array of fine capillary tubes which were arranged with their ends lying on a horizontal line perpendicular to the wall and 0.5 cm below the surface. When the supply of dye was switched on and off small (approximately 0.5 cm) blobs of dye were formed and these were advected by the flow. The displacements (of the order of 5 cm) of many individual blobs measured over a short time interval gave profiles of the downstream velocity (at a fixed distance downstream from the lock) as a function of the time elapsed after the nose passed. The shape and behaviour of these profiles were reproducible in the sense that the measured velocities varied only slowly and smoothly in time and space.

## 3. Qualitative observations

Before discussing the results in detail, we describe the general features of the flow, many of which have not previously been reported. Photographs of both plan and side views of the nose of dyed intrusions at several times after the lock barrier was withdrawn are shown in figure 2 for both wide and narrow locks, while a photograph of the full length of a current after the nose had travelled 106 cm from the lock is shown in figure 3. Photographs such as that in figure 3 reveal no significant qualitative difference between the boundary currents studied here and those produced by Stern *et al.* (1982) with similar density differences and angular velocities, but the photograph is shown here in order to stress two important features not previously acknowledged: extensive and vigorous vertical mixing takes place beneath a large length of the current; and the outer edge of the dyed fresh water represents a well-defined and slowly varying width for the turbulent flow.

Immediately after the barrier is removed the less-dense (dyed) fluid collapses outward over practically the whole lock width. However, before it can move a distance of one Rossby radius it is deflected toward the right-hand wall (rotation is anticlockwise) by Coriolis forces, and, if the lock is wide compared with the deformation radius $R_0 = (g'H_0)^{\frac{1}{2}}/f$, a strong jetlike stream directed toward the wall develops along the front. An associated Coriolis force directed upstream then prevents further motion along the channel everywhere except in the vicinity of the wall. The distance through which the upper layer collapses was found to be close to one deformation radius $R_0$ and the time taken to reach geostrophic balance was of order

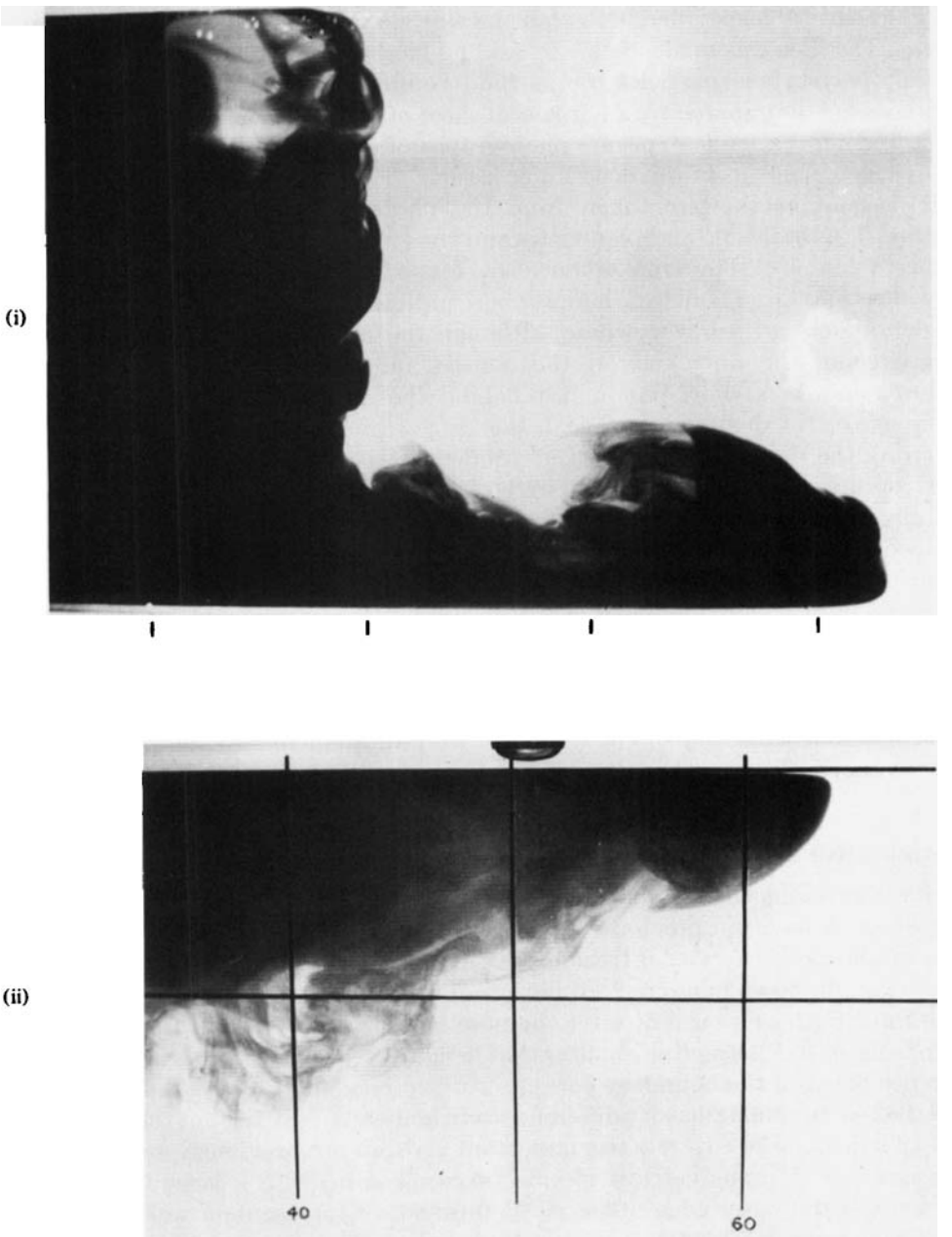


FIGURE 2(*a*). For caption see p. 365.

$f^{-1}$. At the wall there can be no upstream component of the Coriolis force, and a gravity current begins to form as shown in figure 2(*a*). By this stage billows along the whole of the edge of the flow have reached large amplitude and begin to cause mixing between the fluids. However, at the edge of the lock the billows (shown in figure 2*a*) rapidly dissipate and are not replaced, so that the resulting mixing there is limited. Apart from the transient billows, mixing during the early development of

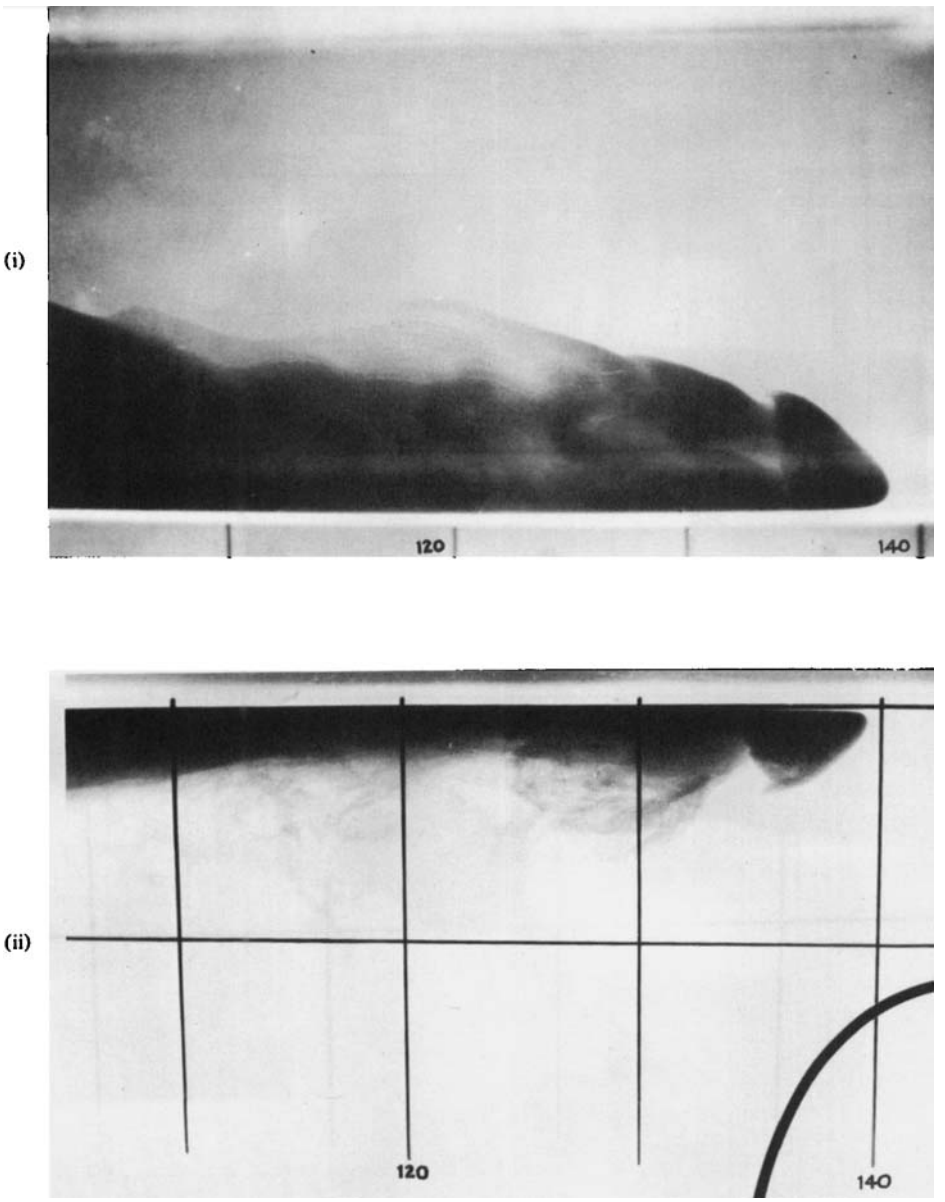


FIGURE 2(*b*). For caption see p. 365.

the flow in the case of 'wide' locks is largely due to the collision of the frontal stream with the wall, which causes the large vertical excursions of dyed fluid seen in the side view on figure 2(*a*), while the wake of the barrier as it is withdrawn produces some small-scale turbulence for all lock widths. These processes too occur only during a very short initial period before the front of the gravity current is fully formed, but might have some influence upon the initial speed of the nose.

Once the boundary current is well developed, the flow has many of the qualitative features predicted by a linear (small depth variation) and long-wave analysis of the problem (Gill 1976). In particular there is a jet-stream along the *left*-hand wall within

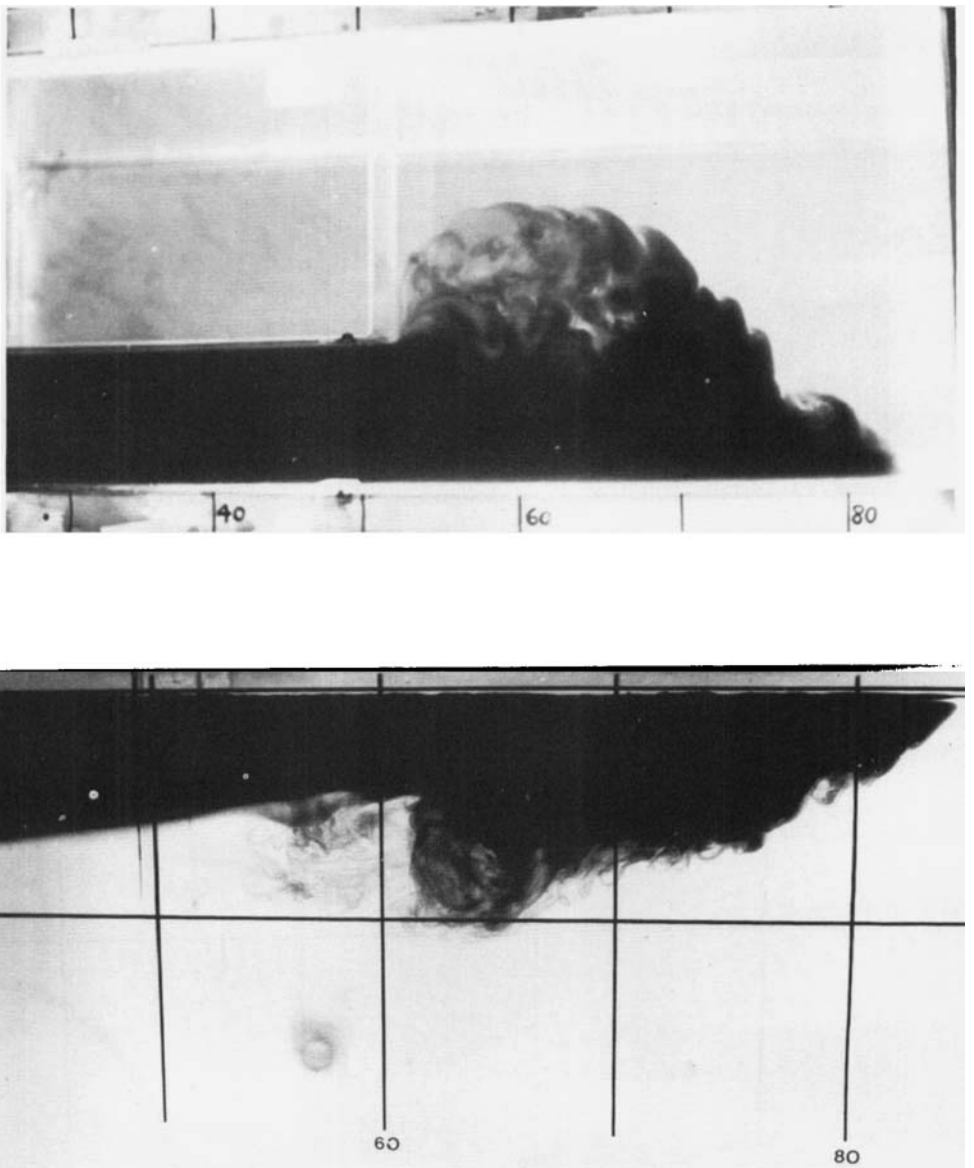


FIGURE 2(*c*). For caption see facing page.

the lock, which then crosses to the right-hand wall near the original barrier position. The resulting flow out of the lock must be hydraulically controlled, with the flow velocity becoming critical at some point near the barrier position. Nonlinear and nonhydrostatic features are also apparent, the current being led by a bulbous 'head' structure (see the photographs in figures 2*b*, *d*) which is similar to that observed in the non-rotating case (Britter & Simpson 1978; Simpson & Britter 1979). As on the non-rotating gravity currents, small billows appear on the leading edge of the nose and grow as they move away from the nose. These billows have their axes aligned roughly across the channel and on the density interface. They break and the resulting

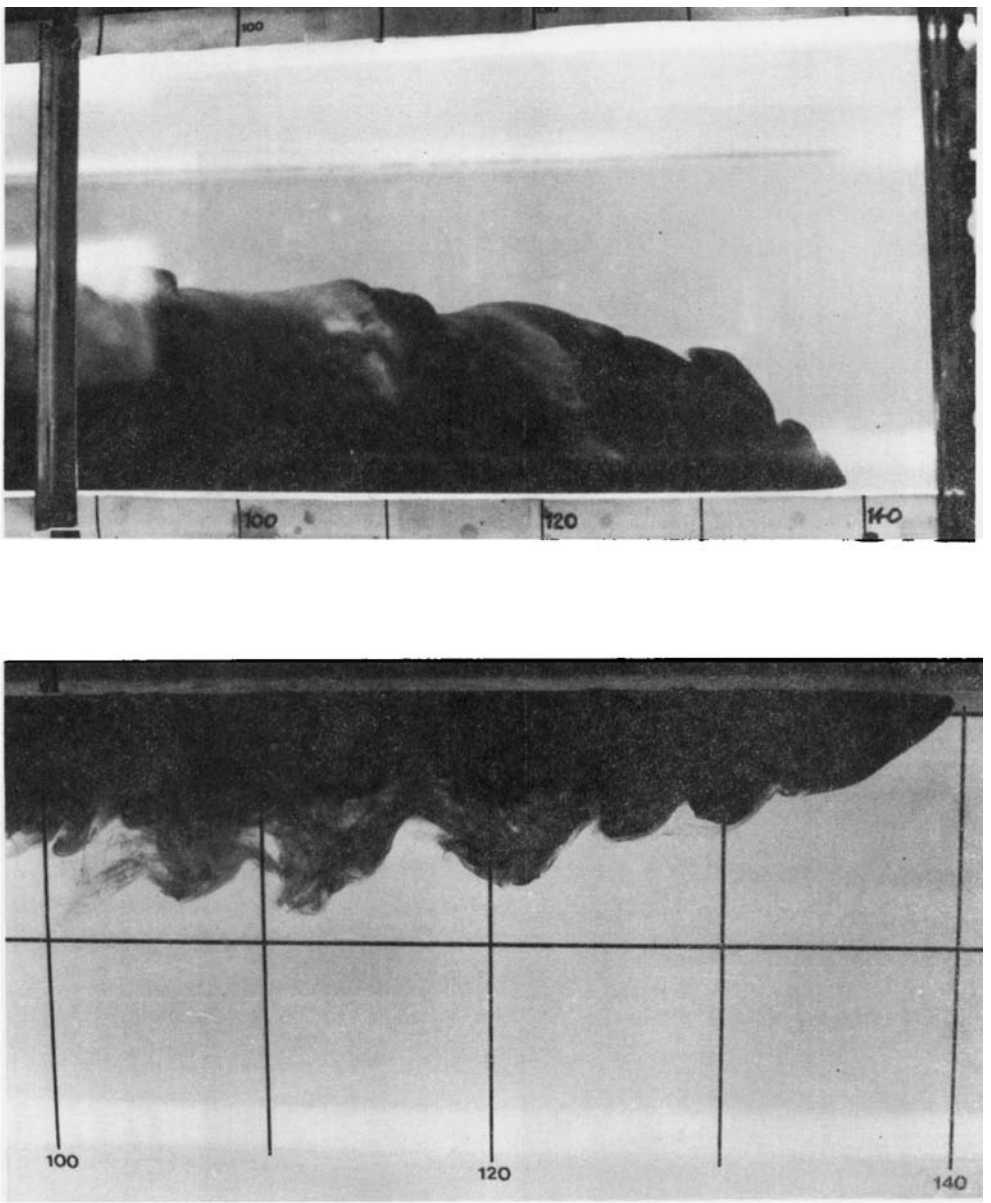


FIGURE 2. Photographs of the nose region of dyed gravity currents in (i) plan and (ii) side view for stages in two different experiments: (*a*) and (*b*) show the same current, produced using lock A, at times (*a*) 20 s and (*b*) 56 s after the barrier was removed ($f = 0.276$ s$^{-1}$, $(g'H_0)^{\frac{1}{2}} = 3.5$ cm s$^{-1}$, Reynolds number $Re_N = 800$); (*c*) and (*d*) show a current produced using lock B at times (*c*) 5.5 s and (*d*) 13.5 s after the flow commenced ($f = 0.495$ s$^{-1}$, $(g'H_0)^{\frac{1}{2}} = 9.9$ cm s$^{-1}$, $Re_N = 1900$). The grid scales on the top and side of the channel wall are 10 cm but photographic enlargements for top and side views are different as these are taken (simultaneously) by different cameras. The bottom of the channel is well below the area photographed. Rotation is anticlockwise.

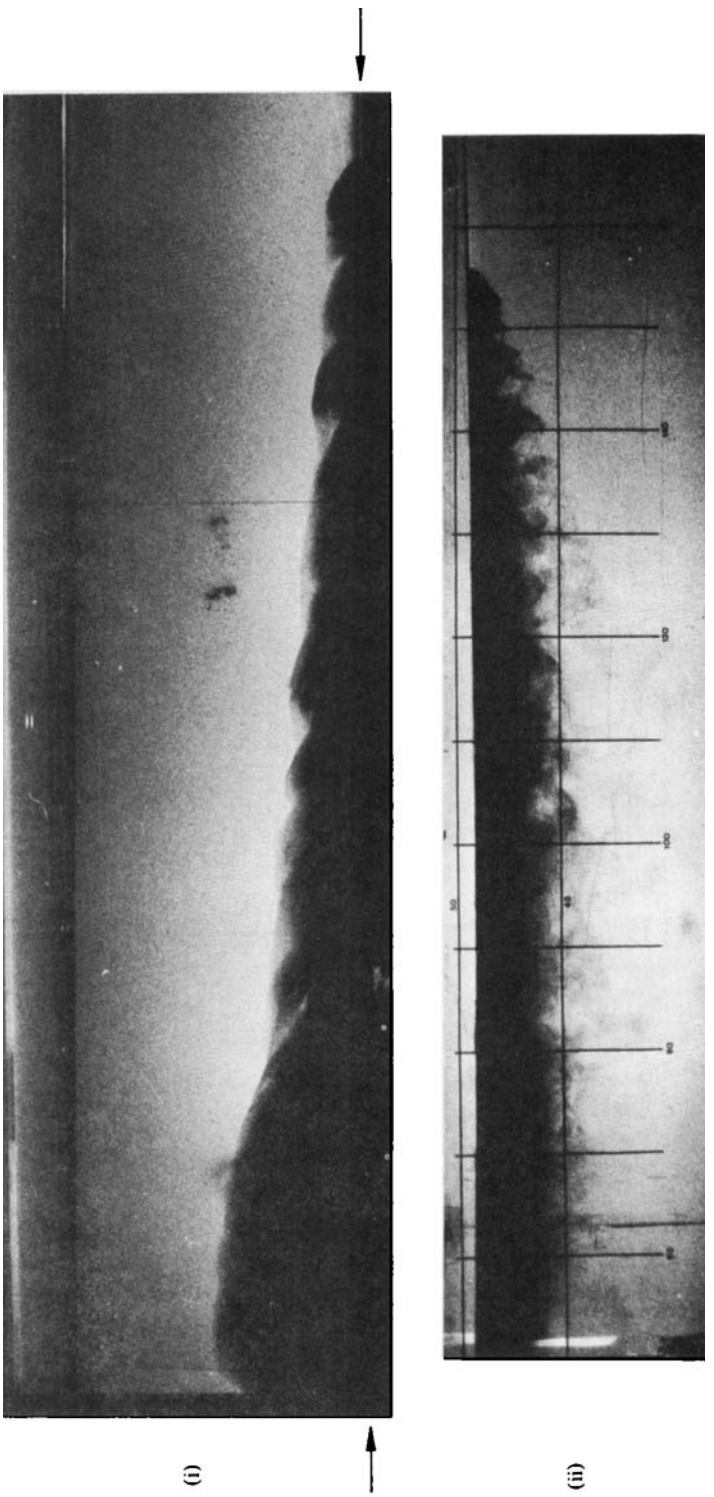


FIGURE 3. A photograph of the full length of a gravity current showing simultaneous (i) plan and (ii) side view. The width of the dyed fluid increases with distances behind the nose. The side view is actually a shadowgraph that reveals density gradients and shows the extent of turbulent mixing beneath the current. The grid scale on the wall is 10 cm. Arrows at the ends of the plan view indicate the position of the wall. The end of the lock can just be seen on the end of both views. Lock B was used, $f = 1.266\ \mathrm{s}^{-1}$, $(g'H_0)^{\frac{1}{2}} = 8.8\ \mathrm{cm\ s}^{-1}$, $\overline{Re}_{\mathrm{N}} = 2800$ and the photograph was taken 10.5 s after withdrawal of the barrier.

turbulence is left behind on the trailing flow. Although eddy velocities tend to dissipate with distance from the nose, plan views show that eddies disturb the full length of the outer edge of the gravity current (as was stressed by Stern *et al.* 1982). Our observations, using both streak photographs and dye, on the other hand, show that eddy motions are also vigorous near the wall. For large Reynolds numbers (figure 2*d*) the eddies cause large vertical excursions of the density interface some distance behind the nose, and our impression is that there is much more vertical mixing than in the equivalent non-rotating flow, with wisps of dyed upper-layer fluid being carried downward into the lower layer within the vortices. Vortex motions a short distance behind the head have their axes partially aligned with the vertical (though the billows were initially nearly horizontal) and cause the fluid to resist the restoring force of gravity. Such vigorous mixing and delayed collapse of the turbulence under gravity often smears out the density (or dye) distribution so that no clear interface can be seen anywhere upstream. Another important point is that cyclonic vortices can be seen to extend into the lower layer. The turbulent motions also appear to become increasingly two-dimensional with distance upstream, giving rise to predominantly horizontal eddy motions.

The flow very close to the nose of the current is not a quasi-steady feature. In most runs, particularly for larger Reynolds numbers, growing billows periodically appear (in both plan and side views) on the leading edge of the head, and the head (or first large billow) breaks up to be replaced by another which is smaller in depth and width. A sequence of such breakdowns is often observed. Unsteadiness of this form does not appear to occur for non-rotating currents.

As the depth of the current decreases with time, so does the propagation speed of the nose. In a few experiments the nose even appeared to stagnate before reaching the end of the channel. This phenomenon was noted by Stern *et al.*, who also reported an associated separation of the flow from the wall. In our experiments no separation occurs. Instead, if the nose depth and velocity become very small, the head structure, billows and turbulence all disappear in a fairly sudden transition and the nose becomes a shallow, narrow viscous intrusion which creeps very slowly along the wall. We have not studied this viscous regime, and no measurements were taken anywhere in the current after the transition of the nose.

Returning attention to the flow in the lock, we noticed that the rapid motion of the fresh water away from the left-hand wall during the early stages of formation of the gravity current initiated a Kelvin wave of elevation on the interface, as predicted by Gill (1976). The wave was seen to travel around the perimeter of the lock (in the anticlockwise direction) and then along the current on the right-hand wall. This is the rotating counterpart to the two-dimensional expansion wave observed in the non-rotating situation, in which case it reflects from the end of the lock and overtakes the nose of the gravity current about ten lock lengths downstream, affecting the subsequent propagation speed of the nose (Rottman & Simpson 1983). In the rotating case, we have only investigated the behaviour of the flow within three lock lengths of the barrier when using the longest lock, and within thirteen lock lengths when using the shortest lock. At the same time, the Kelvin wave must traverse an extra distance corresponding to the lock width. For runs in which the wave was visible we observed that it did not overtake the nose until long after the nose reflected around the far end of the channel. However, the wave was not always visible and it is probable that the expansion eventually overtook the nose for those currents that almost stagnated within the length of the channel.

Associated with the passage around the lock of the Kelvin wave is the formation

of an anticyclonic (clockwise) vortex in the upper-layer fluid within the lock. This vortex motion was very feeble when the deformation radius $R_0$ was larger than the smallest horizontal dimension of the lock, but was strong when $R_0$ was small. A doming of the density interface developed and the vortex effectively trapped much of the remaining fresh water. Only a small continuous flux of fluid was then released to follow the initial boundary current. However, the trapping of fluid cannot influence the propagation of the nose until after the Kelvin expansion wave has overtaken it, and there is no evidence of any dependence of the nose speed upon the existence of the vortex (see §4).

Finally, at a time corresponding to about ten rotation periods after initiation of the flow, unstable long waves became visible on the boundary current near the lock (see figure 19*d*). This was usually long after the nose had reached the far end of the channel, and therefore long after all measurements had been completed. At first only one stationary growing wave could be seen but, later, other waves became visible further downstream, with their amplitude decreasing with distance from the lock and a wavelength which was consistent with $\lambda \approx 6(g'h_u)^{\frac{1}{2}}/f$, where $h_u$ is the local depth at the wall. If the system was left until these waves reached very large amplitude (by which time the nose had come back to the lock), the waves broke toward their upstream side and appeared identical with those studied by Griffiths & Linden (1981, 1982). An anticyclonic rotor developed within the boundary current at each wave crest, along with a cyclonic eddy in the ambient fluid, and extensive horizontal spreading of the buoyant fluid followed. Given the large time- and lengthscales these are clearly rotationally dominated, and possibly quasi-geostrophic, waves.

## 4. Propagation of the nose

The evolution of the flow will first be discussed in terms of the initial conditions and later we will consider local properties of the boundary current. On figure 4 are shown original data for the position $x-x_0$ of the nose, where $x$ is measured from the end of the channel and $x_0$ is the lock length, as a function of time for a sample of experiments using the 20 cm lock length. The position is normalized by $x_0$ and the time by $x_0/(g'H_0)^{\frac{1}{2}}$. It is clear that the nose velocity decreases with time in all cases, at least after a short initial period. However, all attempts to describe the trajectory in terms of one or two simple and common power-law regimes were unsatisfactory. These plots also mask a great deal of useful information.

### 4.1. *Exponential time decay*

Data such as those shown on figure 4 were used to calculate the displacement of the nose and hence its velocity $u_N$ over each time interval. The results, plotted against the distance from the lock barrier, for a sample of experiments are shown on figure 5. The runs shown are typical in that they are chosen simply because they have a similar range of abscissa values for each of the relatively small (figure 5*a*) and relatively large (figure 5*b*) variation of nose velocity. The distance $x-x_0$ from the lock barrier is this time non-dimensionalized by the initial deformation radius $R_0 = (g'H_0)^{\frac{1}{2}}/f$, giving $X = (x-x_0)/R_0$, while the nose velocity $u_N$ is normalized by the velocity $(g'H_0)^{\frac{1}{2}}$, giving $U = u_N/(g'H_0)^{\frac{1}{2}}$. Although this procedure introduces into each data point the errors involved in reading the nose position on the photographic record, it contributes a random uncertainty of only a few per cent. It can now be seen that in each run the velocity quickly increases to a maximum value and then decreases linearly with distance travelled. The straight lines are fitted by a regression

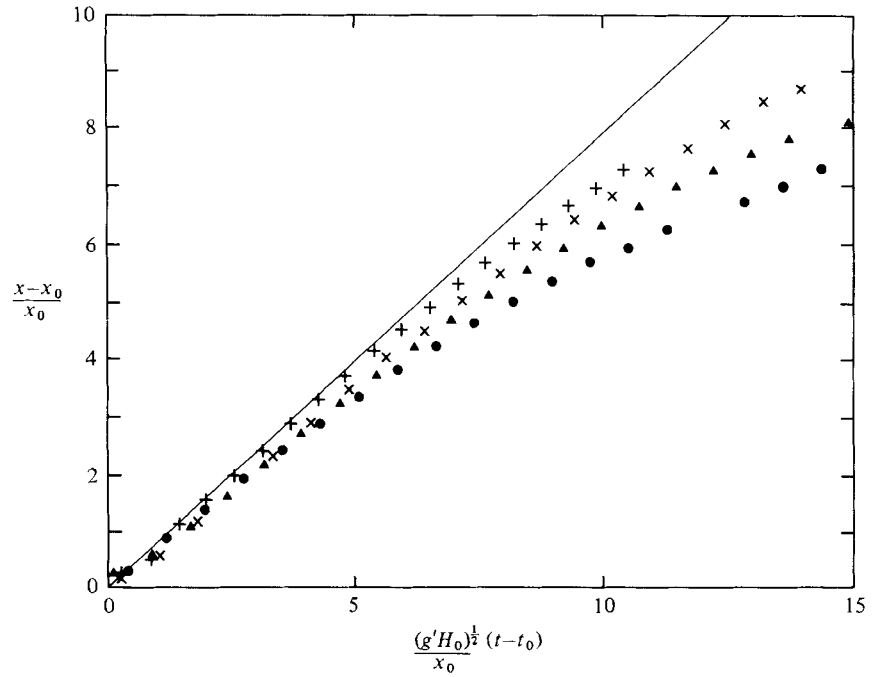


FIGURE 4. Data from a sample of four runs showing the position of the nose relative to the lock barrier (in lock lengths $x_0$) as a function of a dimensionless time after the beginning of the flow at $t_0$. These runs are with lock A ($x_0 = 20$ cm), Coriolis parameters $f = 1.03$ s$^{-1}$ (●), 0.222 s$^{-1}$ (▲), 1.01 s$^{-1}$ (×), and 0.517 s$^{-1}$ (+), depths $H_0 = 9.8$, 3.8, 10 and 8.0 cm and reduced gravities $g' = 0.98$, 6.7, 5.8 and 0.98 cm s$^{-2}$, respectively. For comparison, the straight line represents a constant velocity $u = 0.8(g'H_0)^{\frac{1}{2}}$.

analysis to all points beyond the velocity maximum. Oscillations in the nose velocity, with amplitudes up to 10% of $U$, are also resolved, and these will be discussed in §4.5. For the moment, however, we consider only a smoothed velocity variation, which in all runs is well described by a linear relation in $X$.

For distances beyond the velocity maximum we write

$$U = U_0 - X/\tau, \tag{1}$$

where $U_0$ is the intercept at $X = 0$, and $\tau$ is a constant for each run. Since the velocity is simply $U = \mathrm{d}X/\mathrm{d}T$, where $T = f(t-t_0)$ is the dimensionless time elapsed since the flow began at $\{t = t_0,\ X = 0\}$, the solution to (1) is

$$X = X_{\mathrm{M}}(1 - \mathrm{e}^{-T/\tau}), \quad X_{\mathrm{M}} = U_0\tau, \tag{2}$$

$$U = U_0\,\mathrm{e}^{-T/\tau}. \tag{3}$$

Thus $\tau$ becomes the dimensionless timescale for an exponential decay of the nose velocity. If the empirical relation (1) and its solution (3) were to hold up to large times, then the nose would asymptotically approach the limiting distance $X_{\mathrm{M}} = U_0\tau$ and stagnate.

On figure 6, the nose-velocity calculations that were shown on figure 5 are replotted on a logarithmic scale as a function of the dimensionless time $T$. The time origin $t_0$ was in each case found by linearly extrapolating backwards to $x = x_0$ from the first three measurements of $x(t)$. However, the correction to the timescale was always very

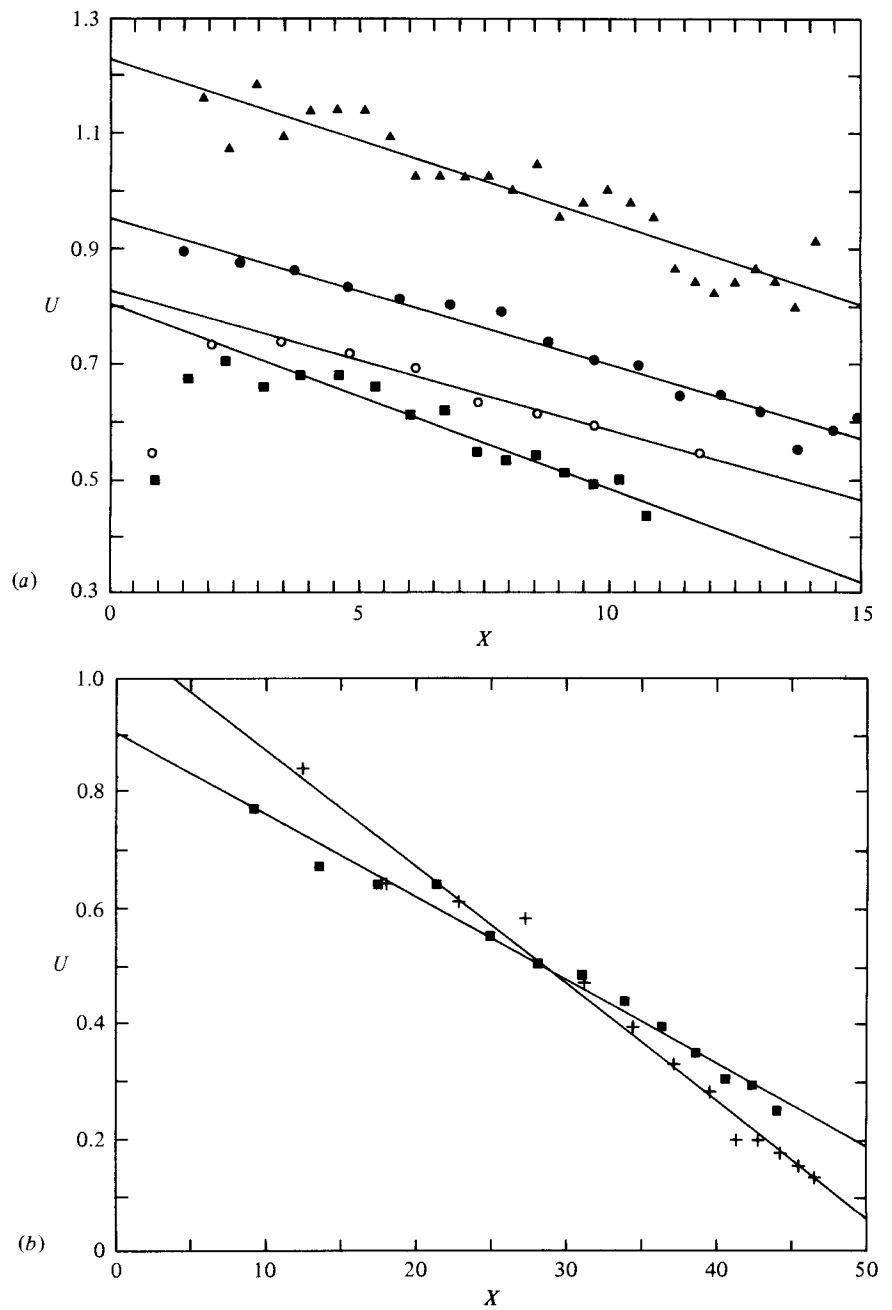


FIGURE 5. Interval-by-interval calculations of the nose velocity $U = u_N/(g'H_0)^{\frac{1}{2}}$ as a function of nose position $X = (x-x_0)/R_0$ for two samples of experiments for which the variation of nose velocity within the length of the channel was (*a*) small and (*b*) large. Note the different velocity scales. Straight lines (1) are fitted to all points beyond that with maximum velocity; their slope is $\tau$ and intercept at $X = 0$ is $U_0$. The run indicated by triangles in (*a*) is shown as an example with large-amplitude oscillations. Parameters here and on figures 6 and 7 are

(*a*) ▲ $f = 1.266$ s$^{-1}$, $(g'H_0)^{\frac{1}{2}} = 8.8$ cm s$^{-1}$, lock B;
● $f = 0.628$ s$^{-1}$, $(g'H_0)^{\frac{1}{2}} = 4.8$ cm s$^{-1}$, lock B;
○ $f = 0.626$ s$^{-1}$, $(g'H_0)^{\frac{1}{2}} = 6.7$ cm s$^{-1}$, lock B;
(*b*) ■ $f = 0.276$ s$^{-1}$, $(g'H_0)^{\frac{1}{2}} = 3.5$ cm s$^{-1}$, lock A;
\+ $f = 1.89$ s$^{-1}$, $(g'H_0)^{\frac{1}{2}} = 5.7$ cm s$^{-1}$, lock C;
■ $f = 2.02$ s$^{-1}$, $(g'H_0)^{\frac{1}{2}} = 7.4$ cm s$^{-1}$, lock C.

All have $\overline{Re_N} > 10^3$ and $E_0 < 10^{-3}$.

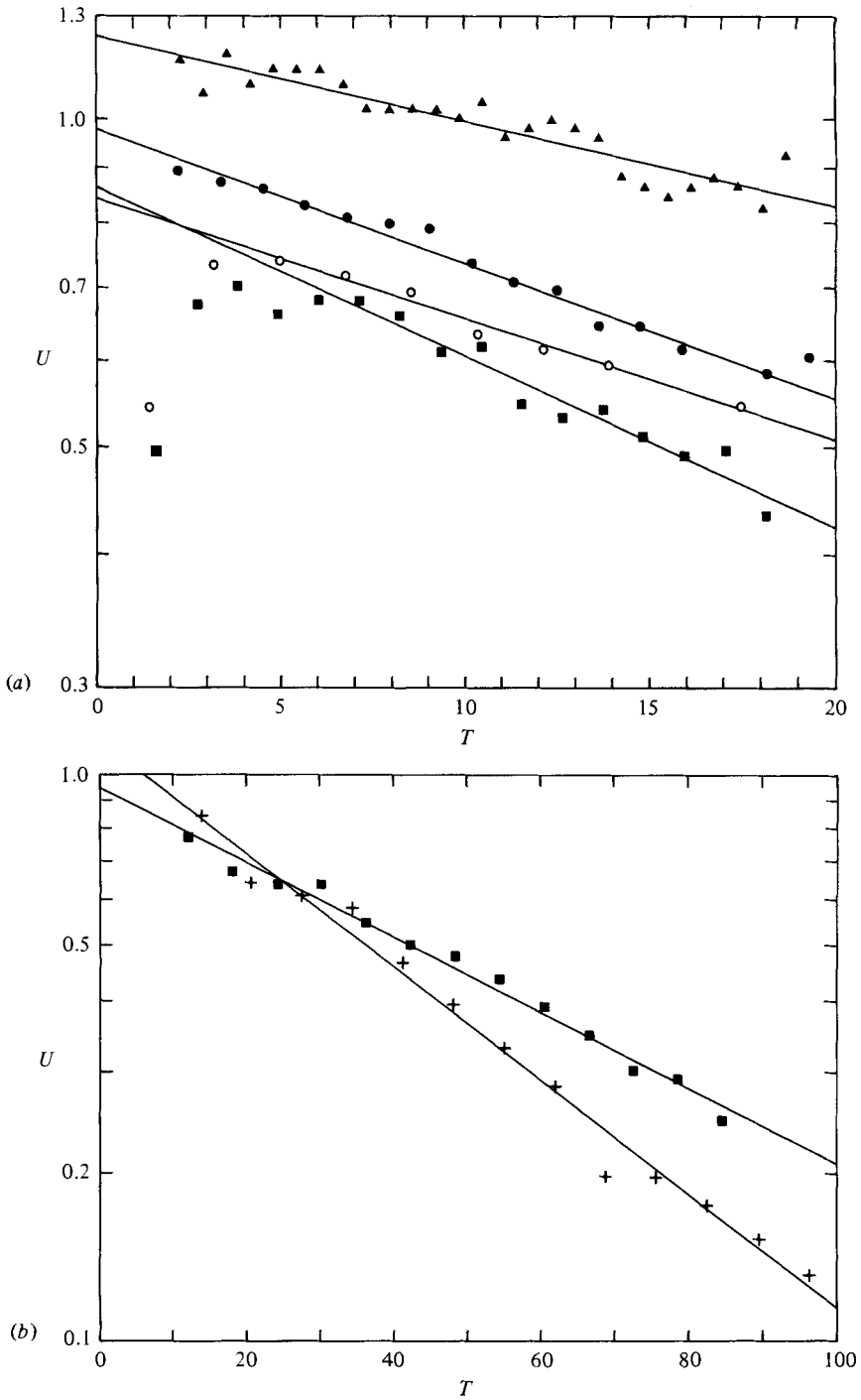


FIGURE 6. The same data for the nose velocity as on figure 5 (same runs) but plotted on a logarithmic scale and as a function of time $T = f(t-t_0)$. Straight lines are fitted exponential decay laws (3). Symbols are as on figures 5 (*a*) and (*b*) for (*a*) and (*b*) respectively. Note the different velocity scales on (*a*) and (*b*).

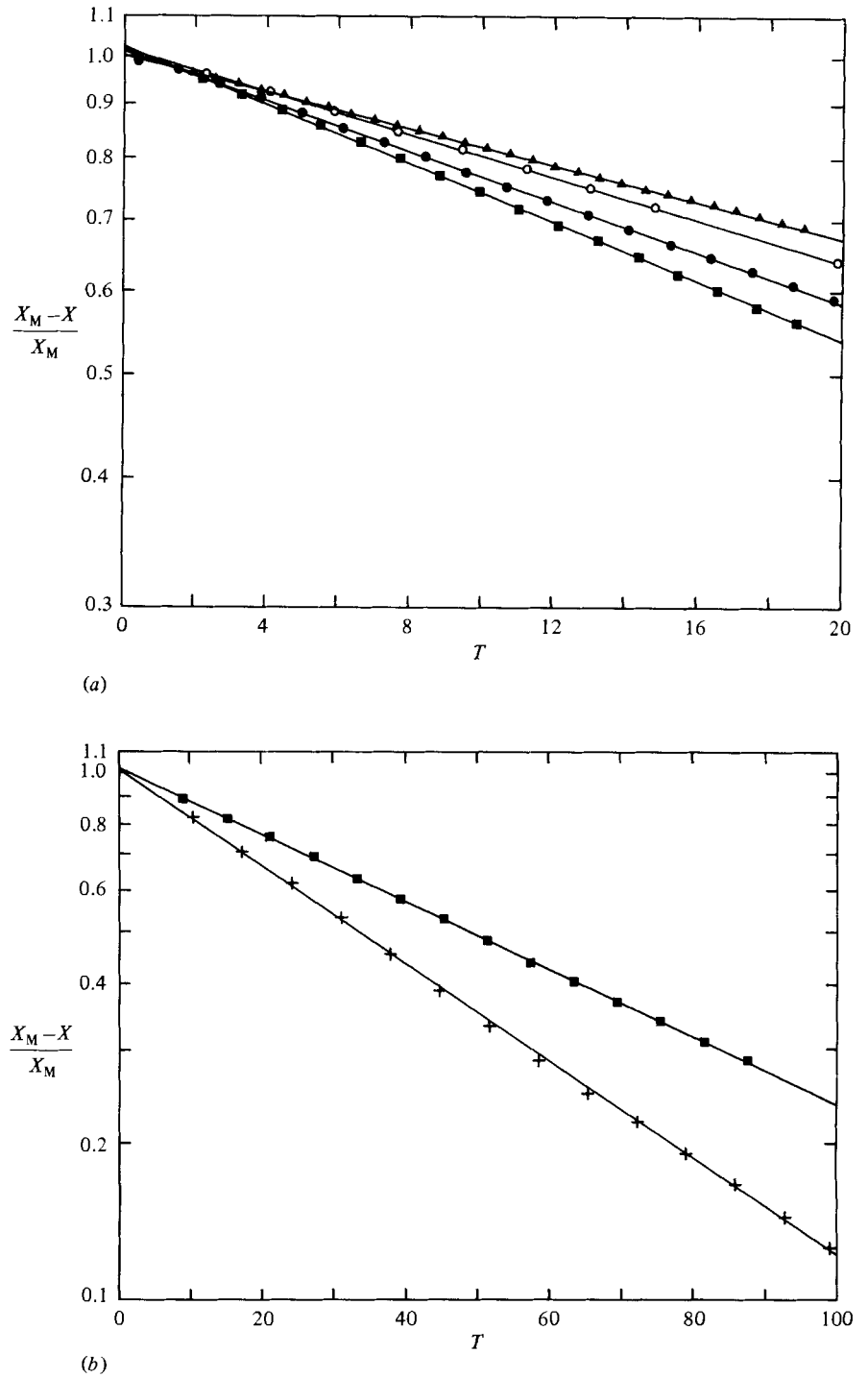


FIGURE 7. The trajectory $X(T)$ for the nose in those runs shown on figures 5 and 6. Straight lines are relation (2) fitted to the points, which are calculated using an empirical value of $X_M$ obtained from the data on figures 5 and 6. Symbols on (*a*) and (*b*) are as on figures 5 (*a*) and (*b*) respectively.

small and less than one time interval. Again the straight lines are fitted by a regression analysis to all points beyond the velocity maximum and show that the exponential (3) gives in every case a good description of the evolution. The velocity sometimes decreases to only 20% of its maximum value before the nose reaches the end of the channel or passes into the viscous regime mentioned in §3. From the data we also find that the initial acceleration phase always takes a time $t_a \approx 5(H_0/g')^{\frac{1}{2}}$, or in dimensionless form $ft_a \approx 5(f^2H_0/g')^{\frac{1}{2}} = 5H_0/R_0$.

Two independent estimates of the values of $U_0$ and $\tau$ were obtained from the fitting of (1) to $U(X)$ and (3) to $U(T)$. The two estimates of the decay time lay within 5% of each other for most experiments (and always within 10%), while the estimates of the velocity intercept $U_0$ were always within 7% of each other. Therefore the mean of the two values of each parameter was used to calculate the maximum travel distance $X_M = U_0\tau$. Then, in order to show that (2) gives a good description of the nose trajectories (see figure 4), the parameter $(X_M - X)/X_M$ is plotted as a function of time. Figure 7 shows such plots for the same runs that are shown on figures 5 and 6, along with the straight lines of best fit. The only significant deviation from the lines again occurs in the initial accelerating phase and the coefficient of regression in over 90% of the experiments exceeds 0.9990. We are therefore confident that the evolution of the flow under all conditions used is well described by an exponential decay law.

### 4.2. *Scaling of the decay time*

The velocity intercept $U_0$ is of order unity for all the experiments, though there is a scatter through the range 0.7–1.3. In the search for the cause of the velocity variation between runs we found that $U_0$ is not reproducible to better than 10% when a given run is repeated and that there is no clear dependence upon any extensive parameter of the system ($R_0/H_0$, $R_0/A_0^{\frac{1}{2}}$, $R_0$/lock width, $H_0/D$, Reynolds number $Re_0 = (g'H_0)^{\frac{1}{2}}H_0/\nu$ and Ekman number $\nu/fH_0^2$). On figure 8 the velocity $U_0$ (obtained with all three lock geometries) is plotted as a function of the initial Reynolds number $Re_0$. No Reynolds-number dependence emerges, and the mean value is $\overline{U_0} = 0.93 \pm 0.14$. This lack of dependence on Reynolds number is consistent with the same conclusion for non-rotating gravity currents, but contradicts the relatively sparse data of Stern *et al.* The scatter is most likely caused by the complex interaction of the frontal stream with the wall, and possibly also the unpredictable mixing, during the early stages of development of the flow.

Of greater interest are the decay timescale $\tau$ and the asymptote $X_M$. On figure 9 the decay time for most runs is plotted as a function of the ratio of the horizontal dimensions of the lock (defined in terms of its horizontal area $A_0$) to the deformation radius $R_0$. A very similar graph is obtained if $\tau$ is replaced by $X_M$. Data obtained with the three different locks are distinguished, but there appears to be no dependence upon the geometry. No other parameter provides a satisfactory collapse of the data and there is a large separation between the data from the different locks if the lengthscale $A_0^{\frac{1}{2}}$ is replaced by either the lock width or length. The parameter $A_0^{\frac{1}{2}}/R_0$ can be thought of as a Froude number since it is the ratio of the velocity scale $fA_0^{\frac{1}{2}}$, the velocity that fluid acquires in moving a distance $A_0^{\frac{1}{2}}$ to escape from the lock, to the wave speed $(g'H_0)^{\frac{1}{2}}$ appropriate for the nose. In other words, it is the square root of the ratio of the initial kinetic energy ($\approx \rho A_0 H_0 \Omega^2 A_0$) of the buoyant fluid due to the rotation of the system to the available potential energy ($\approx \rho A_0 g' H_0^2$). Hence the value of $A_0^{\frac{1}{2}}/R_0$ indicates the influence of rotation upon the hydraulic control of the flow leaving the lock. An alternative view of the parameter is simply that, since the current width scales with $R_0$ (see §5) and the current depth is proportional to $H_0$ (see

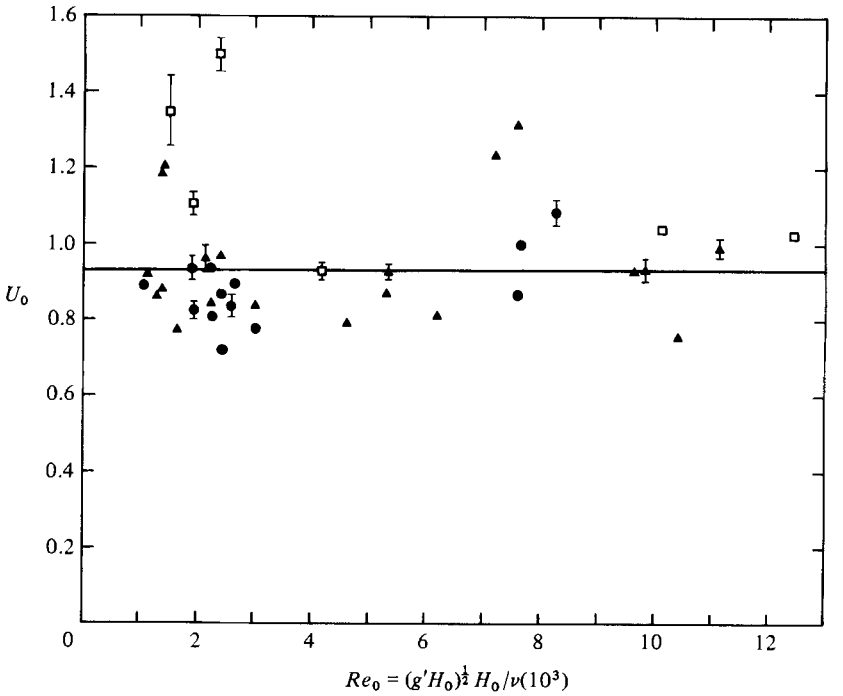


FIGURE 8. The velocity intercept $U_0$ at $\{X = 0, T = 0\}$ from (1) and (3) for all experiments as a function of the initial Reynolds number $Re_0$. The horizontal line shows the mean value $U_0 = 0.93 \pm 0.14$. Symbols indicate the lock geometry: ●, lock A; ▲, lock B; □, lock C (see figure 1). There is no dependence on lock geometry or Reynolds number.

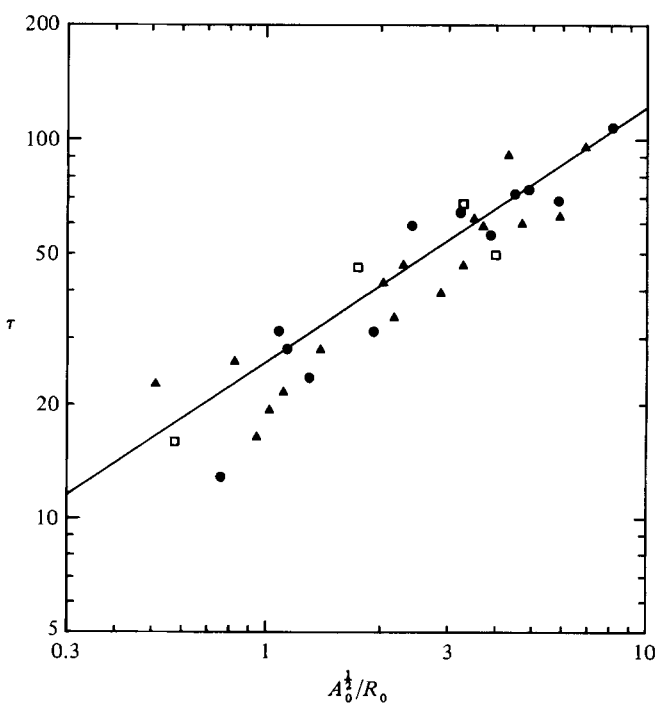


FIGURE 9. The exponential decay time $\tau$ as a function of the Froude number $A_0^{\frac{1}{2}}/R_0$. Only results for runs with Ekman number $E_0 < 2 \times 10^{-3}$ are shown. The straight line has slope $\frac{2}{3}$ and a regression gives a slope 0.69. Each point has an uncertainty of about 10 %. Symbols indicate the lock geometry: ●, lock A; ▲, lock B; □, lock C.

§4.3), then $A_0/R_0$ is the length of a boundary current containing the original volume $A_0 H_0$ of buoyant fluid. The dimensionless length is then $A_0/R_0^2$, upon which should depend both $X_M$ and $\tau$. We therefore define the Froude number $Fr = fA_0^{\frac{1}{2}}/(g'H_0)^{\frac{1}{2}}$.

Returning to figure 9, the straight line drawn has a slope of $\frac{2}{3}$ and gives a satisfactory description of the data (a regression analysis actually gives a slope of 0.69). However, only results from experiments that have small Ekman numbers have been included on figure 9. The influence of viscosity through Ekman dissipation can be brought out by using the trend in figure 9 and plotting, this time for all data, the exponential decay time $\tau$ normalized by $Fr^{\frac{2}{3}}$ against the Ekman number $E_0 = \nu/fH_0^2$.† The result is shown on figure 10(*a*), where we see that the decay time is reduced by Ekman friction (not by low-Reynolds-number effects) when $E_0 > 10^{-3}$. At these conditions the spin-down timescale $E_0^{-\frac{1}{2}}$ becomes as small as the decay time $\tau$ and the initial potential vorticity is dissipated as it is advected downstream. At smaller Ekman numbers the data show no dependence on $E_0$ and the magnitude of the scatter is only twice that expected due to an estimated 10 % uncertainty in calculating $\tau$. Figure 10(*b*) shows the corresponding results for the asymptotic distance $X_M$ normalized by $Fr^{\frac{2}{3}}$. Note that it was only at $E_0 > 10^{-3}$, where $X_M$ is smaller, that the dimensional distance $x_M = R_0 X_M$ lay within the length of the channel and an effectively stagnant nose could be observed. The mean values of $\tau$ and $X_M$ at small Ekman numbers are shown by the straight lines and give

$$\left.\begin{aligned} \tau &= (25 \pm 5)\, Fr^{\frac{2}{3}}, \\ X_M &= (22 \pm 4)\, Fr^{\frac{2}{3}} \end{aligned}\right\} \quad E_0 < 10^{-3}, \tag{4}$$

or in dimensional form $x_M \approx [(g'H_0)^{\frac{1}{2}} A_0/f]^{\frac{1}{3}}$ and $\tau f^{-1} \approx (A_0/g'H_0 f)^{\frac{1}{3}}$. These data show no influence of the ratio of lock width to deformation radius or of the formation of a vortex in the lock, nor is there any detectable correlation with the Reynolds number or the aspect ratio $R_0/H_0$.

### 4.3. *Current depth at the wall*

On the photographs in figures 2 and 3 it can be seen that the depth $h_N$ of the 'head' is the most clearly defined depth that is characteristic of the flow, and as such it gives the best available measure of the time evolution of the current. A spatially averaged (but time-dependent) upstream depth $h_u$ on the wall was also estimated at each time interval, and this is generally about 20 % smaller than that of the head, but the values are less reliable due to large distortions of the interface and to mixing. (The definition of these two depths is included on figure 16, which is a diagrammatic representation of the flow.)

On figure 11 the depth of the head for a sample of experiments is normalized by the initial depth $H_0$ of fresh water in the lock and plotted as a function of the dimensionless distance from the lock. The depth at the position at which a clearly defined heat structure first develops is about $\frac{1}{2}H_0$. It then proceeds to decrease with time in a roughly exponential manner. All other experiments show a similar behaviour, though the measurements of $h_N$ are sometimes distorted by the tendency for the large billow at the rear of the head to form a vortex aligned with the vertical axis of rotation and which tends to carry dyed fluid deeper below the surface.

† The Ekman number is based on the depth $H_0$. This scale is even more important in the rotating system than it is for non-rotating gravity currents. In both cases it determines the depth of the current, but with rotation it also determines the potential vorticity $f/H_0$, which, in the absence of mixing and friction, is conserved by fluid columns as they are carried along the current.

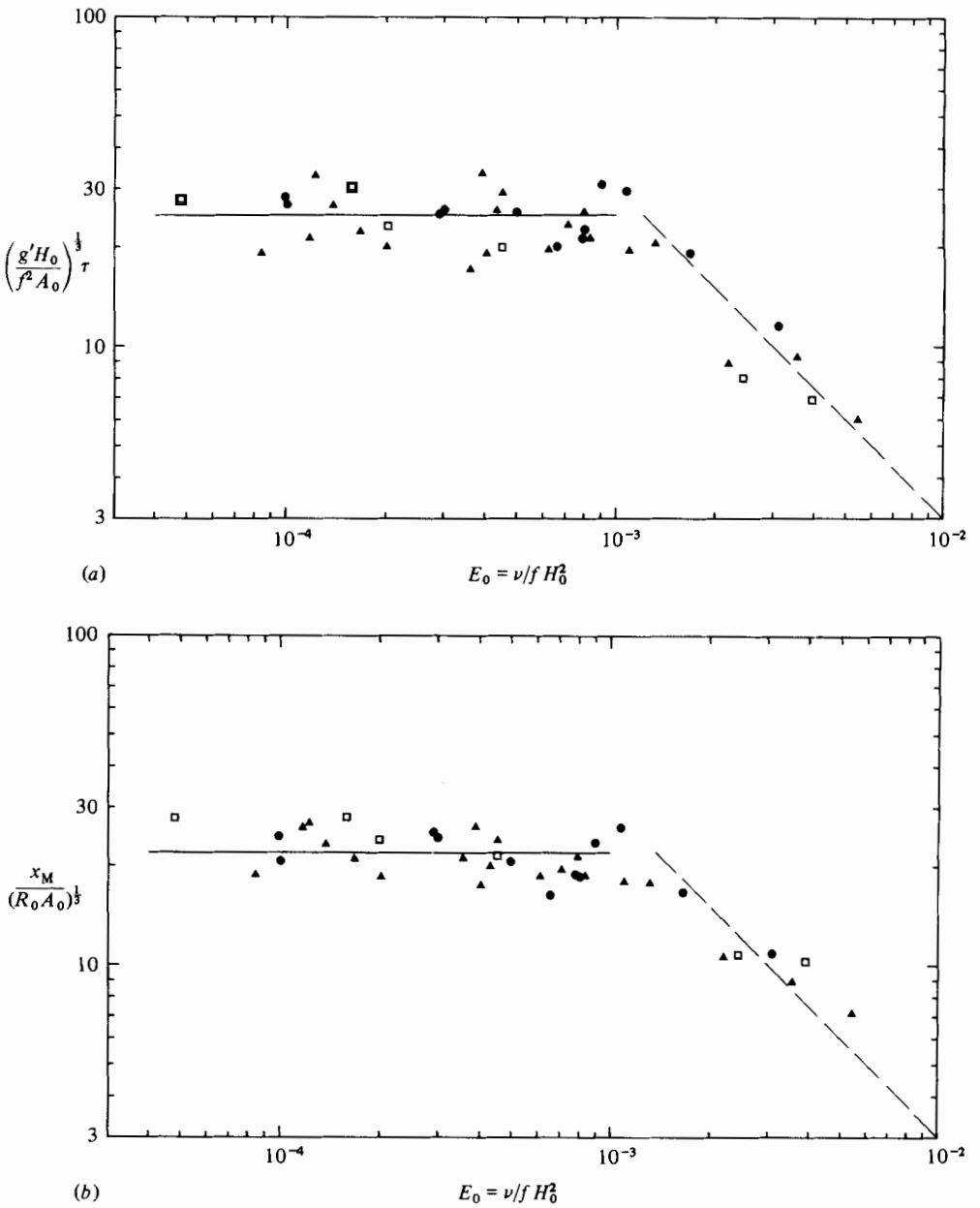


FIGURE 10. Final collective results for all experiments, showing (*a*) the exponential decay time $\tau$ and (*b*) the asymptotic travel distance $X_M = U_0\tau$, both normalized by $(A_0^{\frac{1}{2}}/R_0)^{\frac{3}{2}}$ and plotted against the Ekman number $E_0$. Symbols indicate lock geometry as on figure 9 but show no dependence on this parameter. Horizontal lines show the mean values that give relations (4); the broken lines have slope $-1$.

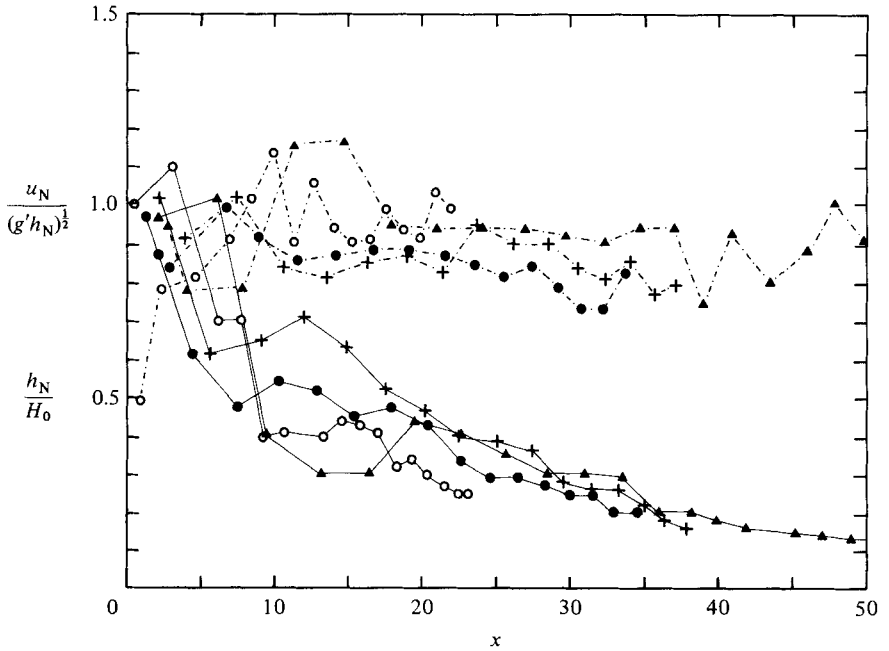


FIGURE 11. The evolution with time of the depth and locally scaled velocity of the nose for several runs. The head depth $h_N$ is normalized by the initial depth $H_0$ in the lock (data points joined by solid lines) and the nose velocity is scaled with $(g'h_N)^{\frac{1}{2}}$ (points joined by broken lines). Each symbol refers to a given experiment.

The temporal variations of the current depth indicate that the measurement technique employed by Stern *et al.*, who averaged all depth measurements taken during each run, conceals much of the behaviour of the system. The decrease of $h_N$ is often steplike, with the steps being due to repeated breakdown of the head, which can be correlated with the growth of new billows on the otherwise smooth leading edge of the nose. The steps in $h_N$ have, at least in some cases, the same frequency as oscillations of the nose velocity (see figure 6) and these oscillations are discussed further in §4.5.

### 4.4. *Local scaling of nose velocity*

Knowing the time-dependent depth of the boundary current, it is possible to investigate the dynamics of the flow near the nose. First, the nose velocity $u_N$ can be compared at each instant in time (see figure 11) with the corresponding local velocity scale $(g'h_u)^{\frac{1}{2}}$ based on the hydrostatic head $h_u$ that provides the buoyancy force to push the nose along (Benjamin 1968; Simpson & Britter 1979). We find that, while the current depth and nose velocity both decrease exponentially in time, $u_N/(g'h_u)^{\frac{1}{2}}$ remains constant to within experimental uncertainty throughout each experiment. The same is true of the more accurately known quantity $u_N/(g'h_N)^{\frac{1}{2}}$, though this sometimes decreases by up to 20 % near the end of runs in which the nose velocity become very small.

The current depth can also be used to define a local Reynolds number $Re_N = u_N h_N/\nu$ which is a more realistic measure of the importance of viscosity than the Reynolds number based on $H_0$. This Reynolds number always begins at a value approximately $\frac{1}{3}Re_0$ and decreases with time, sometimes by as much as an order of magnitude before

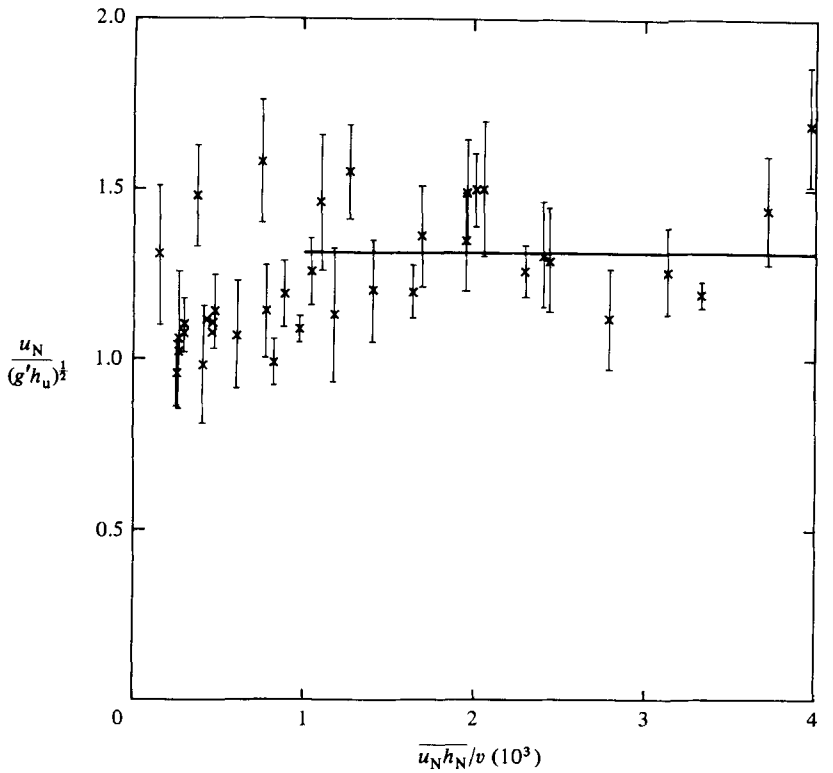


FIGURE 12. The velocity of the nose normalized by the time-dependent scale $(g'h_u)^{\frac{1}{2}}$ (where $h_u$ is the depth far upstream on the wall) plotted against the time average of the local Reynolds number for the nose. Each point shows the mean velocity and its standard deviation for one experiment, the value being nearly constant with time in each run. The mean over all experiments with $\overline{Re_N} > 10^3$ is $1.3 \pm 0.2$.

the nose reaches the end of the channel or becomes a viscous wedge. The latter occurs at $Re_N \lesssim 10^2$. Figure 12 shows the mean dimensionless velocity $\overline{u_N}/(g'h_u)^{\frac{1}{2}}$ for *each* experiment as a function of the time-averaged Reynolds number $\overline{Re_N}$. For runs with small values of the Reynolds number there is possibly some dependence on Reynolds number of the nose velocity. However, although the final value of $Re_N$ in runs with $\overline{Re_N} < 10^3$ often lies in the range 100–200, there is no significant *time* variation of $u_N/(g'h_u)^{\frac{1}{2}}$. For $Re_N > 10^3$ the dimensionless velocity shows no dependence upon Reynolds number and the mean value (shown by the straight line) is $u_N/(g'h_u)^{\frac{1}{2}} = 1.3 \pm 0.2$.† A similar invariance is found for the velocity normalized by $(g'h_N)^{\frac{1}{2}}$, for which the mean value at $Re_N > 10^3$ is $u_N/(g'h_N)^{\frac{1}{2}} = 1.15 \pm 0.1$. We conclude that the Reynolds number has little influence on the dynamics of the flow near the

† The dimensionless velocity of $1.3 \pm 0.2$ is smaller than the value of 1.6 reported by Stern *et al.* (1982) for their largest values of the Reynolds number $Re_0$ ($\approx 8 \times 10^3$, noting that their Reynolds numbers are incorrect by a factor of ten) because they calculated the velocity using an initial value of $u_N$ obtained near the beginning of each run, as well as a time-averaged value of $h_u$. Stern *et al.* also predicted a Froude number of 1.54–1.58, but see § 7.3. The corresponding Froude number for the nose of non-rotating gravity currents on a rigid bottom (at the same fractional depth $h_u/D \approx 0.05$–$0.1$) is measured to be 1.1–1.2 with no slip on the bottom and 1.5–1.7 with slip (Simpson & Britter 1979). The value appropriate to a free-surface intrusion is likely to be closest to that with slip.

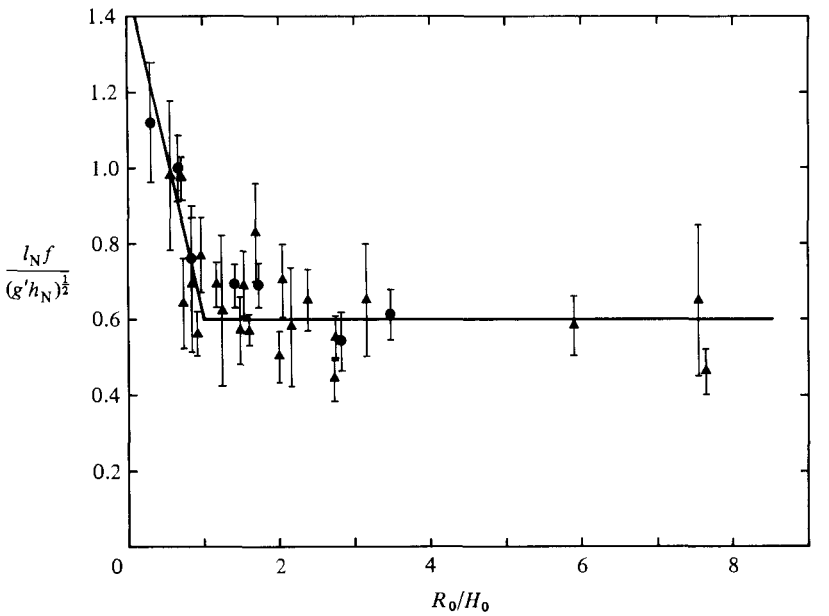


FIGURE 13. The head width $l_N$ for each run, normalized by the local time-dependent deformation radius $(g'h_N)^{\frac{1}{2}}/f$, as a function of the initial aspect ratio $R_0/H_0$. Error bars show the standard deviation about the mean for many measurements within each run. Straight lines show the mean width $l_N = 0.6(g'h_N)^{\frac{1}{2}}/f$ for $R_0/H_0 > 1$ and a fit to data for $R_0/H_0 < 1$. Symbols indicate the lock geometry as on figure 9.

nose just as it does not significantly affect the measured exponential decay timescale $\tau$, though it may contribute slightly to the scatter of the data on figure 10 due to the inclusion of some experiments with low Reynolds numbers.

### 4.5. *Width of the nose*

An interesting quantity is the width of the intruding nose. This we define as the maximum width (shown on figure 16) of the head at times when it is not in the process of breaking up. The maximum depth $h_N$ occurs at the same $x$-position, and the ratio $fl_N/(g'h_N)^{\frac{1}{2}}$ remains constant with time in each experiment to within 20%, with no clear systematic variation.

On the other hand, the value of the dimensionless width is not the same in all experiments. On figure 13 the widths $fl_N/(g'h_N)^{\frac{1}{2}}$ for all experiments are plotted as a function of the aspect ratio $R_0/H_0$. The error bars show the standard deviation for a large number of individual width measurements taken throughout an experiment, and it should be noted that the initial aspect ratio (the square root of the parameter $g'/f^2H_0$ used by Stern *et al.*) is being used to give a rough description of the local but time-dependent ratio $l_N/h_N$. For 'wide' currents ($R_0/H_0 > 1$) the width of the head is a constant fraction ($0.6 \pm 0.1$) of the local deformation radius. However, it increases with decreasing aspect ratio when $R_0 < H_0$. This variation is similar to that found by Stern *et al.* (1982) for an average current width behind the nose. Since larger vertical accelerations are likely to occur for smaller aspect ratios, they attributed the increase in width to non-hydrostatic effects. However, in geophysics it is the very large aspect ratios that are of interest, and under this condition the constant width $fl_N/(g'h_N)^{\frac{1}{2}} \approx 0.6$ characterizes the intruding nose as well as the trailing current for a distance of many nose widths upstream. Note that this width implies that the

cross-stream slope of the density interface at the head is much greater than that which could be in geostrophic balance with the Coriolis force due to the velocity $u_N$.

A Rossby number $Ro_N = u_N/fl_N$ for the motion of the nose can now be evaluated. Using the above result for $l_N$ and the velocity $u_N = 1.15(g'h_N)^{\frac{1}{2}}$ we have $Ro_N \approx 2.0$, a value that is independent of time and all external parameters whenever the aspect ratio $R_0/H_0 > 1$ and the Reynolds number is not too small. Hence for aspect ratios greater than unity the nose width can be written as $l_N \approx u_N/2f$, a value equal to the maximum possible width for the steady, frictionless limiting bore predicted by Stern (1980) and Stern *et al.* (1982) (see appendix A of Stern *et al.*). Going a step further, the nose velocity $u_N = 1.3(g'h_u)^{\frac{1}{2}}$ implies that $l_N \approx 0.65(g'h_u)^{\frac{1}{2}}/f$, a value slightly smaller than the predicted maximum width $(g'h_u)^{\frac{1}{2}}/f\sqrt{2}$. Hence Stern's limiting bore appears to have been realized, though caution is needed in the numerical comparison because the predictions are based on a long-wave (i.e. hydrostatic) approximation while the observed 'head' and large billows beneath the current are produced by non-hydrostatic effects (irrespective of the ratio of current width to depth).

### 4.6. *Instability and velocity oscillations*

Since the oscillations in the absolute velocity $U$ sometimes have amplitudes as great as 10 % of $U$, it is of interest to discuss their frequency. This is relevant to the nature of the billows that have such a large effect upon both the structure and, as is argued in §8, the dynamics of the flow. However, we have not studied in detail the stability of the flow at the nose, but briefly present here data that are readily obtained from the photographs and velocity measurements.

The similar appearance of side views of rotating and non-rotating gravity currents suggests that we compare the growth rates and dimensions of the billows on each, while keeping in mind that the basic flow is different in at least some respects. For the non-rotating case, Britter & Simpson (1978) report that the time taken for each billow to grow to its maximum amplitude scales with the parameter $\Delta U/g'$, where $\Delta U$ is the velocity difference that gives rise to the billow. At large Reynolds numbers they find $g't^*/\Delta U \approx 3$. For the rotating case, direct observations of the flow and measurements of the nose depth suggest that each breakup of the head corresponds to the growth of a new billow. Hence we roughly equate the period of oscillation of the nose velocity with the time taken by a billow to grow, and we plot on figure 14 a dimensionless oscillation period using the mean nose velocity $\overline{u_N}$ as a function of the mean local Reynolds number $\overline{Re_N}$. Data are shown for all those runs that exhibited one or more clear oscillation cycles, while runs shown as squares are considered circumspectly because the oscillation period in these cases was an integer multiple of the inertial period $2\pi/f$ and oscillation amplitudes tended to be greater, suggesting an inertial resonance within the channel.

At small Reynolds numbers the dimensionless period increases rapidly with decreasing Reynolds number until one oscillation period surpasses the time taken by the nose to travel the length of the channel. The head of the current then appears to be a very stable and only slowly varying feature. We conclude that viscous effects reduce the growth rate of the billows. At large Reynolds numbers ($\overline{Re_N} > 10^3$), on the other hand, the oscillation period appears to become independent of Reynolds number. There is a large scatter ($\pm 30$ %) in the data, but we expect some of this to be due to a dependence upon the cross-stream slope of the density interface (given by $R_0/H_0$) and other variations in the basic flow at the nose. The mean value at $\overline{Re_N} > 10^3$ is $g't^*/\bar{u}_N = 6.7 \pm 2.3$, and in order to compare this growth time with that given by Britter & Simpson we can follow their approach to estimate the velocity

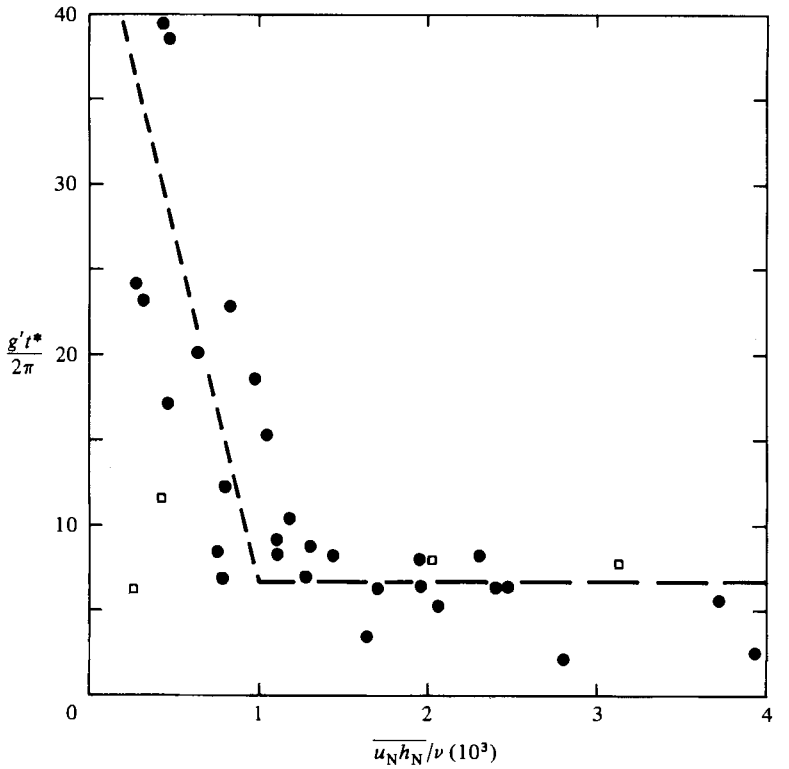


FIGURE 14. The dimensionless period $g't^*/\bar{u}_N$ for observed oscillations of the nose velocity as a function of the mean local Reynolds number. This period could not be measured in all runs. The squares show oscillations that may be due to inertial resonances. Lines show the mean period $g't^*/\bar{u}_N = 6.7 \pm 2.3$ for $\overline{Re}_N > 10^3$ and a fit by eye to the data for $\overline{Re}_N < 10^3$.

difference $\Delta U$. First, the fluid velocity near the wall within the intrusion is greater than the nose speed ($\approx 1.3u_N$ according to information obtained some distance upstream, see §5.1). Secondly, the environment fluid on the wall at the position where the billows are growing moves relative to the nose at a velocity $\approx -1.5u_N$ (see Britter & Simpson). Therefore $\Delta U \approx 2u_N$ and billows in the rotating case have $g't^*/\Delta U \approx 3.3 \pm 1$, in accord with the result for non-rotating currents.

Three further properties of the flow provide useful comparisons: the angle included by the density interface on the leading edge of the head and the free surface, in a sample of ten runs, lay in the range 35°–48°; the ratio of the maximum amplitude of billows to their wavelength lay between 0.5 and 1.0; and the ratio of billow amplitude to current depth $h_u$ took values from 1.0 to 3. All of these results are identical with those reported by Britter & Simpson, and, along with the measured oscillation periods, lead us to conclude that the background rotation and the three-dimensional structure of the boundary currents do not significantly alter the flow on the sidewall very close to the nose or the accompanying shear instability. The instability is of the Kelvin–Helmholtz type and is not a rotationally dominated phenomenon as implied by Stern *et al.* (1982). This result can be understood when we see that the oscillation period discussed above, if rescaled by the rotation period, lies in the range $0.05 \leqslant ft^*/4\pi \leqslant 0.25$ (or $0.1 < f\bar{u}_N/g' < 0.6$) for large Reynolds numbers. Thus rotation does not affect the shear instability simply because the growth rate of billows is much greater than the rotation rate $\Omega$. Billows begin to be

strongly influenced only after they have reached their maximum amplitude and broken.

So far we have mentioned only the dimensions and growth rate of large-amplitude billows. A guide to whether the background rotation is of importance in determining the conditions under which the nose is unstable, or the position on the leading edge at which waves begin to grow, is given by the linearized stability analysis for a sharp density interface in a rotating system (Chandrasekhar 1961; Huppert 1968). Noting that this analysis assumes uniform horizontal flow in each layer and a horizontal interface, it establishes that rotation is always stabilizing but has negligible effect if $2\Omega^2/\gamma g' \ll 1$, where $\gamma$ is the horizontal wavenumber. Assuming that the billow wavelength on the gravity currents scales with current depth $h_u$, the criterion becomes $g'/f^2 h_u \gg 1$ or, equivalently, $R_0/H_0 \gg (h_u/H_0)^{\frac{1}{2}}$. For currents with $R_0/H_0 < 1$, this result is not valid as the assumptions of the analysis are then far from being satisfied. However, for wide currents we can be confident that rotation plays no stabilizing role.

## 5. Upstream flow structure

### 5.1. *Velocity profiles*

Velocities far behind the nose were measured as a function of time at a fixed distance of 60 cm downstream from the lock barrier. Only lock B was used for these measurements. Consistent results were obtained from four experiments with different rotation rates and initial depths $H_0$ but all having large local Reynolds numbers ($\overline{u_N h_N}/\nu \approx 2 \times 10^3$), small Ekman numbers ($E_0 < 10^{-3}$) and large aspect ratios ($R_0/H_0 \geqslant 1$). Profiles of the downstream velocity at four selected times for one experiment are shown on figure 15, where the cross-stream distance $y$ is non-dimensionalized by the absolute scale $R_0 = (g'H_0)^{\frac{1}{2}}/f$, and the fluid velocity is normalized by the absolute scale $(g'H_0)^{\frac{1}{2}}$. The elapsed time $\Delta T = f(t-t_N)/4\pi$ is given in rotation periods, where $t_N$ is the time at which the nose passed the observation position and $t$ is the mean time in the short interval required for the velocity measurement. The arrows on the ordinate at the right indicate the velocity $U$ of the nose at the times of the first and last profiles shown (upper and lower arrows respectively). The arrow on the abscissa near the end of each curve indicates the measured position of the outer edge of the fresh water (which was dyed with a colour different from that of the small blobs used for velocity measurements). Velocity profiles obtained at intermediate times show a slow variation of the profile, and we are confident that these profiles truly represent the mean flow. Time-exposure photographs showing the motion of neutrally buoyant particles reveal consistent profiles.

For a short time of the order of 0.1 rotation periods after the nose had passed the observing position, the injected dye mixed rapidly within the current (both in the vertical and horizontal) and no velocity measurements were possible. After this period, however, vertical motions were negligible compared with horizontal motions, and velocities normal to the wall were less than 10 % of the downstream components (this can also be seen in figure 19*c*). The first profile shown on figure 15 is at $\Delta T = 0.13$. At times close to this, flow in all of the runs consists of a streamwise velocity $u = (1.3\text{–}1.5)\,U$ at positions very close to the wall. The velocity has a maximum near the wall at $y \approx 0$ and falls to $u = U$ at a distance $y/R_0 \approx 0.2$ from the wall. However, the consequent mass flux toward the nose rapidly disappears with time, because in

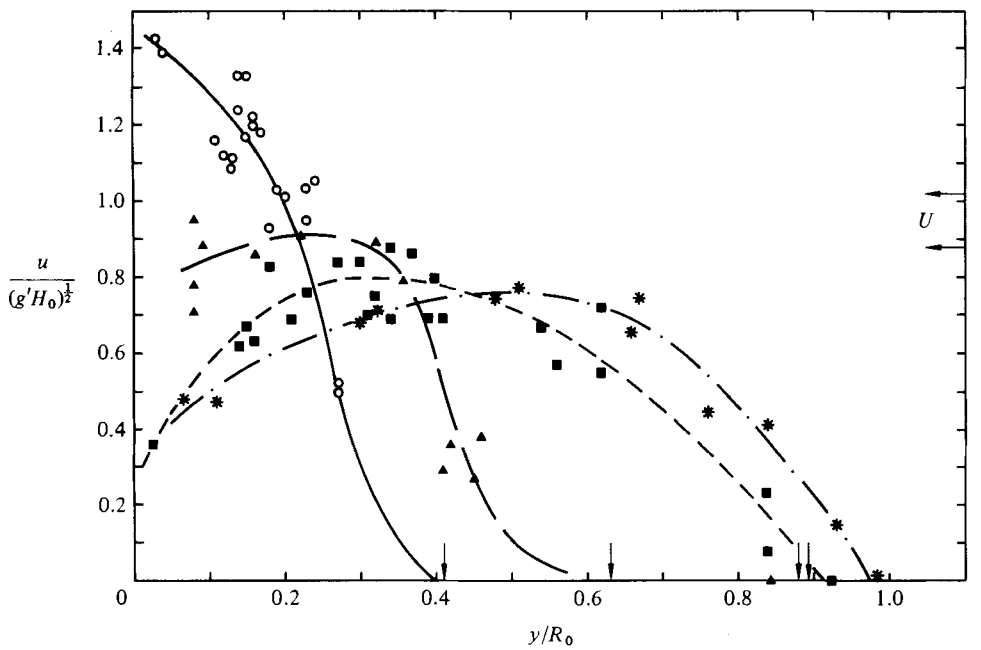


FIGURE 15. Four cross-stream profiles of the flow velocity for one experiment, taken 60 cm from the barrier of lock B at various times after the nose passes: ●, $T = 0.13$, ▲, 0.31, ■, 0.46, *, 1.3 rotation periods. Lines are drawn by hand through the data. The wall is at $y = 0$ and the position of the edge of the dye (which was clearly defined) is shown by an arrow near the end of each curve. Horizontal arrows at right show the nose velocity $U$ at the times of the first (upper arrow) and last (lower arrow) profile. The deformation radius $(g'h_N)^{\frac{1}{2}}/f$ for the head when it passed the observing position was $0.65R_0$ and the head width was $0.38R_0$.

all runs the maximum flow velocity becomes smaller than the nose velocity after a time $0.25 \lesssim \Delta T \lesssim 0.6$. The second profile shown is at $\Delta T = 0.31$, by which time the maximum has already moved a considerable distance from the wall. The later profiles on figure 15 are at $\Delta T = 0.46$ and $\Delta T = 1.31$ and show a further broadening of the current along with a steadily decreasing flow velocity on the wall. For each profile the position of the outer edge of the (dyed) fresh water corresponds closely with the position at which the measured streamwise velocity falls to zero and beyond which no motion was detected. The current width is discussed further in §5.3 and implications of the velocity profiles for the mass flux along the current are examined in §5.2.

The broadening of the current and reduction with time of the velocity on the wall are not due to wall friction since this would create only a very thin boundary layer of thickness $(\nu t)^{\frac{1}{2}}$, which will have grown to $0.06R_0$ in the time $\Delta T = 1.3$. The broadening must be due in part to diffusion of momentum by the horizontal eddy motions. The decrease of the wall velocity and migration of the velocity maximum, though, must be the result of an adjustment of the flow toward a steady, geostrophic boundary current with uniform potential vorticity $f/H_0$ and no variation in the streamwise direction. A similarity solution for such a laminar current was given by Stern (1980) and Stern *et al.* (1982). More simply, it can readily be shown from the equations for geostrophic balance and conservation of potential vorticity that the relative vorticity $-\mathrm{d}u/\mathrm{d}y$ of this ideal flow must be negative and the velocity and

depth profiles hyperbolic (Griffiths & Linden 1982). Maximum depth then occurs at the wall, and maximum velocity at the outer edge. With the presence of eddy motions, though, the laboratory currents remain far from this ideal solution throughout the observation period.

Reflection of the expansion wave in the lock must be considered when measuring velocities far upstream. If the speed of this wave is taken to be a constant $(g'H_0)^{\frac{1}{2}}$ relative to the local fluid velocity (though it will actually decrease as the depth of the upper layer decreases), we calculate for the experiment of figure 15 that it cannot reach the measuring position 60 cm from the lock until a time $\Delta T > 0.9$ after the nose has passed. Hence the first three profiles shown (and possibly also the last) were measured before the expansion arrives.

### 5.2. *Mass flux relative to the nose*

The measured velocity profiles indicate that the maximum flow velocity at the fixed observing position and just beneath the free surface became less than the nose velocity only a short time after passage of the nose. To an observer moving with the nose this implies that, beyond a certain distance upstream, mass is being carried away from the nose at all positions across the stream. An evaluation of the streamwise position at which the net mass flux toward the nose falls to zero would require measurements of the depth profiles simultaneous with the velocity profiles. However, it is clear that the intrusion consists of a slug of fluid from which there is a net mass loss, the mass being removed largely near the outer edge of the current (see first profile on figure 15). Hence the nose must continually decrease in size, as was directly observed. This result stands in contrast with the behaviour of two-dimensional non-rotating gravity currents in which mass is carried toward the nose at a rate that balances the detrainment (mixing) of fluid into the ambient layer, a balance that can produce a steady flow. In the presence of rotation the effective 'detrainment' of buoyant fluid (see below) is much greater because fluid is left behind near the outer edge of the flow behind the nose. However, this additional horizontal 'detrainment' does not explain the unsteadiness since, in the absence of other effects, the nose velocity would be expected to rapidly adjust until a steady balance was achieved. An explanation of the unsteadiness is offered in §7.3.

A more general and illuminating description of the upstream structure, this time in terms of the distance behind the nose, can be extracted from data such as that on figure 15. The time $t-t_N$ can be interpreted as a measure of the distance $d$ from the nose to the observation position, which in terms of the initial deformation radius is

$$d/R_0 \approx f(t-t_N)\,U, \tag{5}$$

where the time-dependent nose velocity $U(t)$ is known for each run and takes values $U \lesssim 1$. More directly, we can measure the distance from the nose to the measurement position at the time at which measurements are taken. However, in interpreting data taken at one particular distance from the lock in terms of the distance behind the nose, it must be remembered that we assume an approximate self-similarity of the flow over the time period $t-t_N$, and it is not clear how accurately the results will describe the flow at times when the nose is much further from the lock. Nevertheless, it is at least a qualitatively useful approach and gives a reasonable picture of the laboratory currents for times during which the nose is within the length of the channel. Thus the profiles shown on figure 15 were taken at distances 2.1, 3.8, 6.2 and 15.9 deformation radii $R_0$ behind the nose.

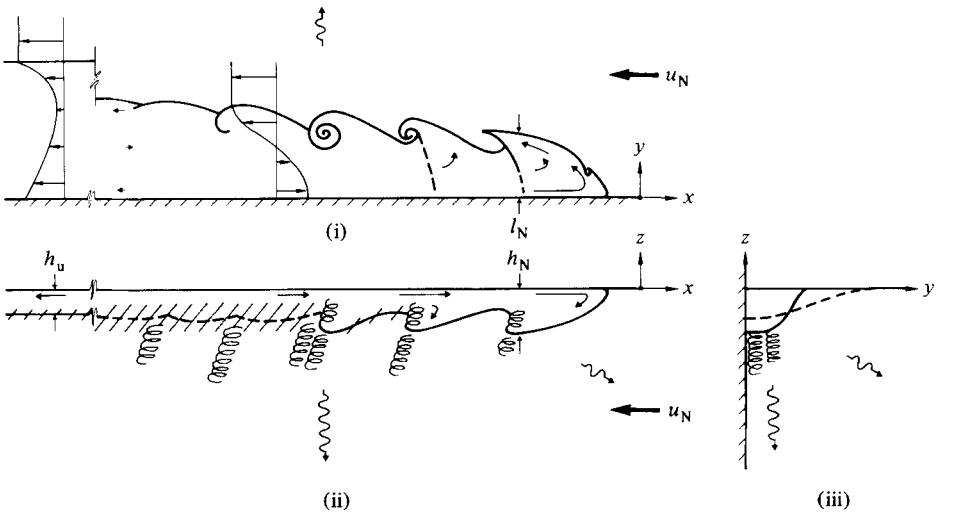


FIGURE 16. Sketch of the flow relative to the nose in the boundary current at one instant in time: (i) plan view; (ii) a vertical plane parallel to and close to the wall; (iii) cross-section as viewed from the end of the channel. The details of flow in the head and billows is highly unsteady and the billows on the interface extend from the wall to the edge of the current. Velocity profiles are based on measurements such as those shown on figure 15, the rest from particle motions. The definition of measured head depth $h_N$, head width $l_N$ and upstream depth $h_u$ are shown. Instability of the nose, mixing beneath the current and radiation of inertial waves are indicated.

Having a description of the flow as a function of distance behind the nose, we are now in a position to give an overall diagrammatic representation of the flow relative to the nose of the boundary current. In order to do this it is useful to assume that the flow relative to the nose is only slowly varying in time (see §7). On figure 16 are sketched the streamlines and profiles of velocity relative to a reference frame moving with the nose, along with an indication of the spatial dependence of the structure of the flow. Since the flow is everywhere turbulent, the downstream velocities shown must be considered as mean local values. Figure 16(i) represents the flow in a horizontal plane near the surface, (ii) the flow in a vertical plane near the wall at $y = 0$, and (iii) the cross-sectional shapes of the nose (solid curve) and upstream current (broken curve). The latter qualitative shapes are derived only from direct observations through the end of the channel. In anticipation of observations presented in §6 we have also included in this sketch the radiation of inertial waves, which must occur in such a system. The formation of billows and cyclonic vortices, along with their influence on vertical mixing beneath the current, are indicated in (ii) and (iii), though the plan views of surface flow taken alone would suggest that eddies exist only near the outer edge of the current. As indicated in (i) the billows develop in curved lines across the density interface and appear at the current edge more as horizontal billow or eddy motions.

In all runs we find that the maximum fluid velocity relative to the nose becomes negative at a distance within the range $3 < d/R_0 < 7$ upstream of the nose. This behaviour was not noticed by Stern *et al.* (1982), whose observations concentrated upon a region within about $10R_0$ of the intruding nose. Another difference from the description of the flow given by Stern *et al.* is that our streak photographs and direct observations of particle motions show that there is no dividing streamline that could be used to define the width of the flow near the nose. Neglecting a very thin viscous

boundary layer on the wall, the only stagnation point on figure 16 is at $y = 0$, and all motions normal to the wall are directed *away* from the wall. The maximum streamwise velocity also occurs on the wall. We must therefore be careful when discussing 'detrainment' of fluid from the current since, in the sense of Stern *et al.* *all* of the fluid (and not just that outside a dividing streamline) is now detrained as it approaches the nose. On the other hand, most of the fluid that moves away from the nose near the outer edge or bottom interface of the flow remains to take part in the boundary current, with the eddies retaining a translational velocity, and only a relatively small amount of fluid is actually mixed with the lower layer. No estimate of the effects of this true detrainment due to mixing have been possible and more quantitative information on the space and time dependence of the net mass (or salt) flux along the current would require simultaneous measurements of velocity and depth profiles.

### 5.3. *Upstream current width*

From velocity profiles such as those shown on figure 15 it is possible to define several widths to characterize the flow. We can also use the outer edge of the upper-layer fluid (made visible by dye), which appears to be clearly defined and is easily measured. This is also a useful quantity for comparison with geophysical observations as it gives the complete width of the turbulent current. At the same time, the velocity profiles far upstream reveal a significant mean streamwise velocity all the way to the edge of the dye. On the other hand, Stern *et al.* argued that only an inner laminar region of the current should be considered for the purpose of comparison with their dynamical model of the flow and, in their experiments, chose to measure the distance from the wall to a line of maximum shear. This distance was then averaged over time and space (but not too close to the nose and not 'at very large distances upstream') for each run.

On figure 17, three different definitions of the width (all measured 60 cm from the lock barrier) for four different experiments are plotted against the time $\Delta T = f(t-t_N)/4\pi$ elapsed after passage of the nose past the measuring position. The filled symbols show the position of the outer edge of the dye at the surface, the open symbols the position of the maximum velocity gradient and the crosses and asterisks the position of the velocity maximum. The dye edge always corresponds closely with the position at which the downstream velocity vanishes. The absolute scaling of $y$ by the deformation radius $R_0$ is retained and the experiments have $R_0 = 5.4, 7.8, 11.7$ and 35.4 cm. The scale $d/R_0$ is included to show distance behind the nose but is only approximate as each run has a slightly different velocity $U$. No velocity profiles could be taken at $\Delta T < 0.1$ due to rapid turbulent motions within the current, but the width of the head ($l_N \approx 0.38R_0$ at this measuring position for these runs) is shown by the letter 'N' at $\Delta T \approx 0.03$.

As the current propagates along the channel, all three characterizations of the width increase with time. After about one rotation period ($\Delta T > 0.8$), or ten deformation radii behind the nose, the widths appear to approach asymptotes that place both the outer edge of the dye and the maximum shear at $y \approx R_0$ and the maximum velocity at $y \approx 0.5R_0$. Since the head width is $l_N \approx 0.38R_0$ in these runs, the total width of the flow at the observation position increases by almost a factor of three after the head passes.

Such variations of width suggest that the previous averaged estimates of the distance from the wall to the line of maximum shear underestimate the width far upstream. The mean width $\overline{l_u}$ found by Stern *et al.* satisfied $\overline{l_u} \approx 0.42(g'\overline{h_u})^{\frac{1}{2}}/f$, where

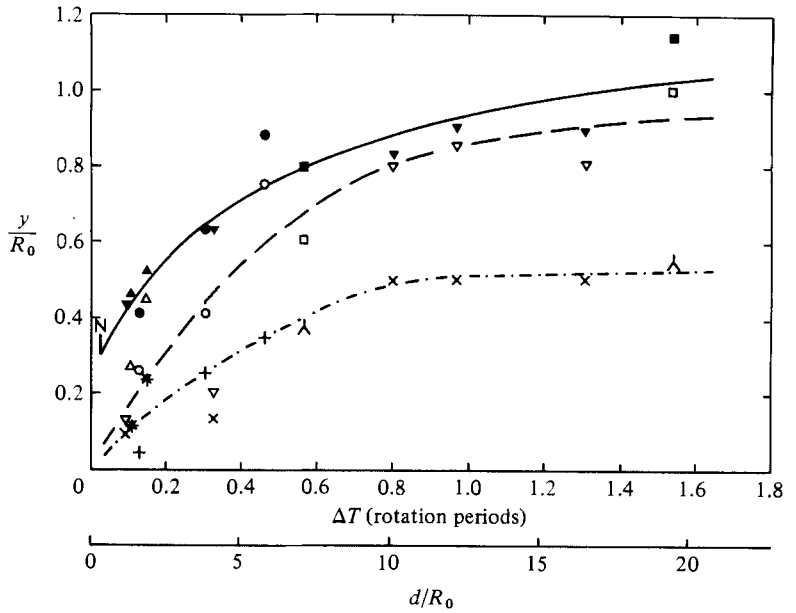


FIGURE 17. The width of the boundary current at a fixed distance of 60 cm from the lock barrier for four runs with different Rossby radii but similar initial velocities as a function of tine elapsed after the nose passes that position. Time is given in rotation periods $4\pi/f$. A second scale shows the approximate distance from the measuring position to the nose as found from (5) by using the mean value of $U$ for the four runs. Filled symbols show the outer edge of the dye at the surface (——), open symbols the position of maximum shear (– – –) and other symbols the position of the velocity maximum (—·—·—). Parameters are

$$R_0 \begin{cases} \bigcirc, \bullet, +, & R_0 = 11.7 \text{ cm}, (g'H_0)^{\frac{1}{2}} = 7.5 \text{ cm s}^{-1}; \\ \square, \blacksquare, \lambda, & R_0 = 7.8 \text{ cm}, (g'H_0)^{\frac{1}{2}} = 7.9 \text{ cm s}^{-1}; \\ \triangle, \blacktriangle, *, & R_0 = 35.4 \text{ cm}, (g'H_0)^{\frac{1}{2}} = 8.0 \text{ cm s}^{-1}; \\ \triangledown, \blacktriangledown, \times, & R_0 = 5.4 \text{ cm}, (g'H_0)^{\frac{1}{2}} = 8.1 \text{ cm s}^{-1}. \end{cases}$$

$\bar{h}_u$ is a space and time average of the upstream depth at the wall. For comparison, taking $h_u < \frac{1}{2}H_0$, the data on figure 17 indicate that $l_u \approx R_0 > 1.4(g'h_u)^{\frac{1}{2}}/f$ at a distance $10R_0$ behind the nose. If the flow had been measured at a position further from the lock then the local depth $h_u$ would have been smaller and the above comparison even worse. On the other hand, the average of Stern *et al.* was strongly biased toward positions within ten initial deformation radii behind the nose and their data, when replotted, show a linear increase of dimensionless width $f\bar{l}_u/(g'h_u)^{\frac{1}{2}}$ with increasing channel (or observation) length measured in deformation radii $R_0$. These variations of width were attributed to non-hydrostatic effects at small aspect ratios, but they are also likely to have been a result of the spatial and temporal variations of width observed here. In any case, given the averaging procedure the data are consistent with ours.

## 6. Radiation of inertial waves

Disturbances that contain frequencies less than $2\Omega$ will create inertial waves in a rotating fluid. The group velocity of a wave with frequency $\omega$ and wavelength $\lambda$ is $C_g = (\Omega\lambda/2\pi)\cos\theta$ directed at an angle $\theta = \sin^{-1}(\omega/\Omega)$ to the vertical. Thus the intrusion of the nose of the boundary current, the formation of billows and eddies

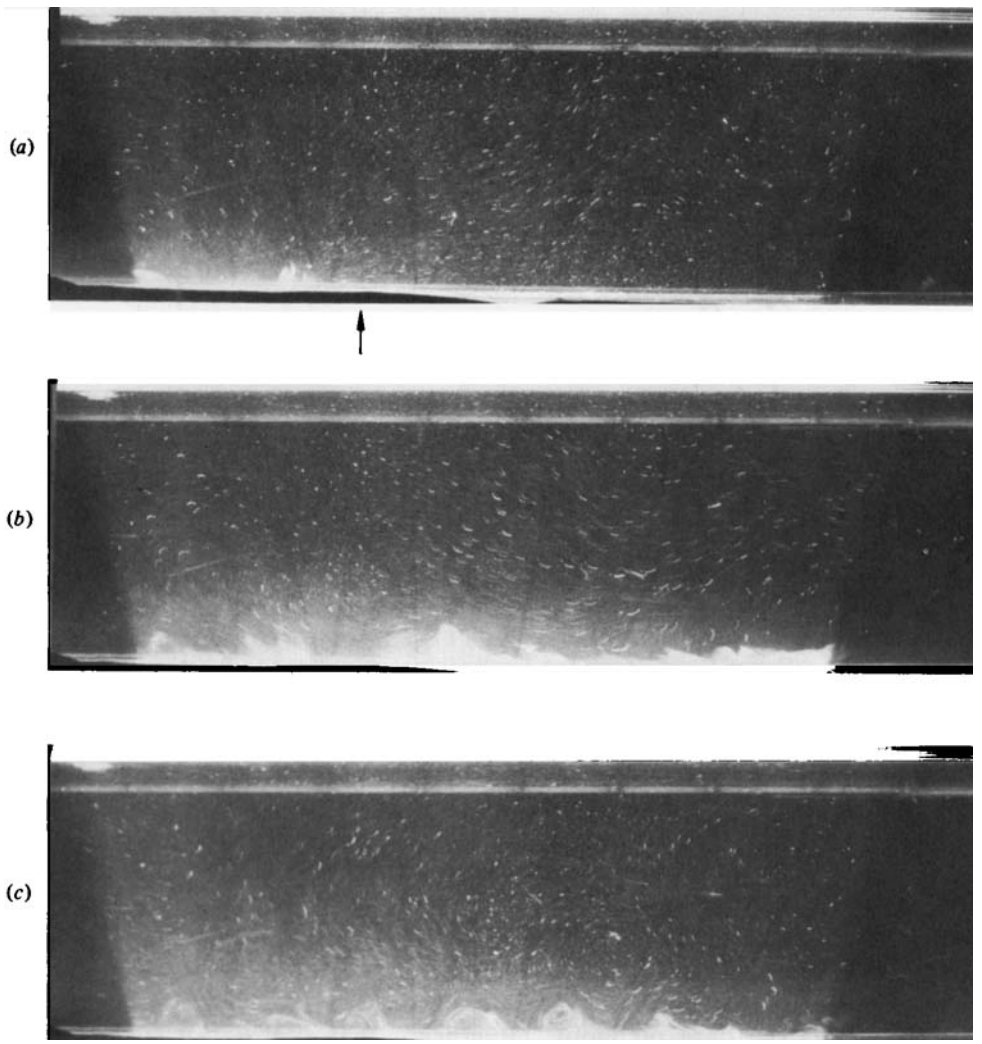


FIGURE 18. Time-exposure photographs of particles in a horizontal sheet of light 11–13 cm (or three current depths) below the free surface showing wave-like and eddy motions in the deep lower layer. The viewing section is 80 cm long and begins 30 cm from the lock barrier. Rotation is anticlockwise and flow moves from left to right. Wisps of fluorescein dye are entrained from the upper-layer current (with head depth $h_N \approx 4$ cm) and make visible the cyclonic vortices beneath the current. Photographs were taken (*a*) 0.36, (*b*) 0.77 and (*c*) 1.15 rotation periods after the opening of the lock. An arrow marks the position of the nose in (*a*) and (*b*), but it is 50 cm past the viewing section in (*c*). The streaks reveal that velocities in the lower layer are $\approx 10\,\%$ of the velocity of the current. Total exposure time 3.0 s (including the dot at the end of each streak); $f = 0.680\ \mathrm{s}^{-1}$; $(g'H_0)^{\frac{1}{2}} = 7.6\ \mathrm{cm\ s}^{-1}$.

and the subsequent translation of these structures will produce a broad spectrum of inertial waves which can propagate ahead of the nose, away from the wall and deep into the lower layer (as indicated on figure 16). In order to detect any consequent motions we have taken time-exposure photographs of neutrally buoyant particles in the deep lower layer.

On figures 18 and 19 are shown two sequences of time-exposure photographs taken

in plane view. Particles are in each case illuminated by a horizontal sheet of light about 2 cm thick. On figure 18 the sheet of light is positioned 11–13 cm (or about three head depths $h_N$) below the free surface. At this level wavelike motions are visible well before the nose arrives in the viewing section (*a*), though the particles were stationary before the lock was opened. Stronger motions directed outward from the nose (*b*) appear as the nose passes and the lower layer contains more random eddy motions once the nose has travelled 50 cm (or ten head widths) past the viewing section (*c*). Particle velocities here are of the order of 10% of the nose velocity. In (*c*) there are also relatively strong vortices close to the wall 50–100 cm upstream from the nose. These have been made more visible by adding a small amount of fluorescein dye to the upper layer, small wisps of which are entrained downwards into the vortices below the interface.

For figure 19 the horizontal sheet of light is positioned just 1–3 cm below the surface, and particles are in both fluids. The lower layer this time contains a small amount of fluorescein so that the outer edge of the upper layer can be seen. The nose of the current is not distinct as the exposure must be long to reveal the relatively small velocities in the lower layer. At this level no motion is detected well ahead of the nose but there is again a stream flowing forward and outward from the nose (*a*, *b*) in a manner that is quite different from the flow about bodies in a nonrotating system. There is again a mixture of eddy and wavelike motions in the lower layer 0.5–1 rotation period after the nose passes (*c*) and the velocities are about 10–20% of the nose speed. As mentioned in §5.1, particle velocities within the current are almost parallel to the wall, though there is some evidence of the presence of eddies. The photograph in figure 19 (*d*) was taken at a much later time (7.9 rotation periods after removal of the lock barrier) at which the nose had almost returned to the lock along the opposite wall of the channel. It is included to show the growth of rotationally dominated waves, which are long compared to the current width, at large times and very large distances behind the nose.

Though the particle velocities in the deep lower layer a short distance behind the nose are small, they occur throughout a volume of fluid that is at least an order of magnitude greater than the volume of the current itself. The many wavelike and eddy motions created by the passage of the gravity current therefore contain a significant amount of kinetic energy. Furthermore, while the small cyclonic vortices are confined to the wall, they extend through the interface and many current depths into the lower layer, thereby tending to couple the two layers together and exerting a drag on the upper-layer flow. In §7 we investigate the influence upon the flow of the drag due to vortices and radiation of inertial waves.

## 7. Dynamics of boundary currents

### 7.1. *The momentum equation*

By considering the flow along a streamline that lies on the wall at $y = 0$, the conservation of momentum in a hydrostatic approximation can be written as

$$\frac{\partial u}{\partial t} + g' \frac{\partial h}{\partial x} = -u \frac{\partial u}{\partial x} - \frac{F_\Omega}{\rho}, \tag{6}$$

where $u$ is the fluid velocity parallel to the wall and $F_\Omega/\rho$ is a contribution (per unit mass) to the drag due to the presence of rotation. Thus $F_\Omega$ is the wave drag due to inertial waves and columnar vortex structures (the latter can be thought of as being

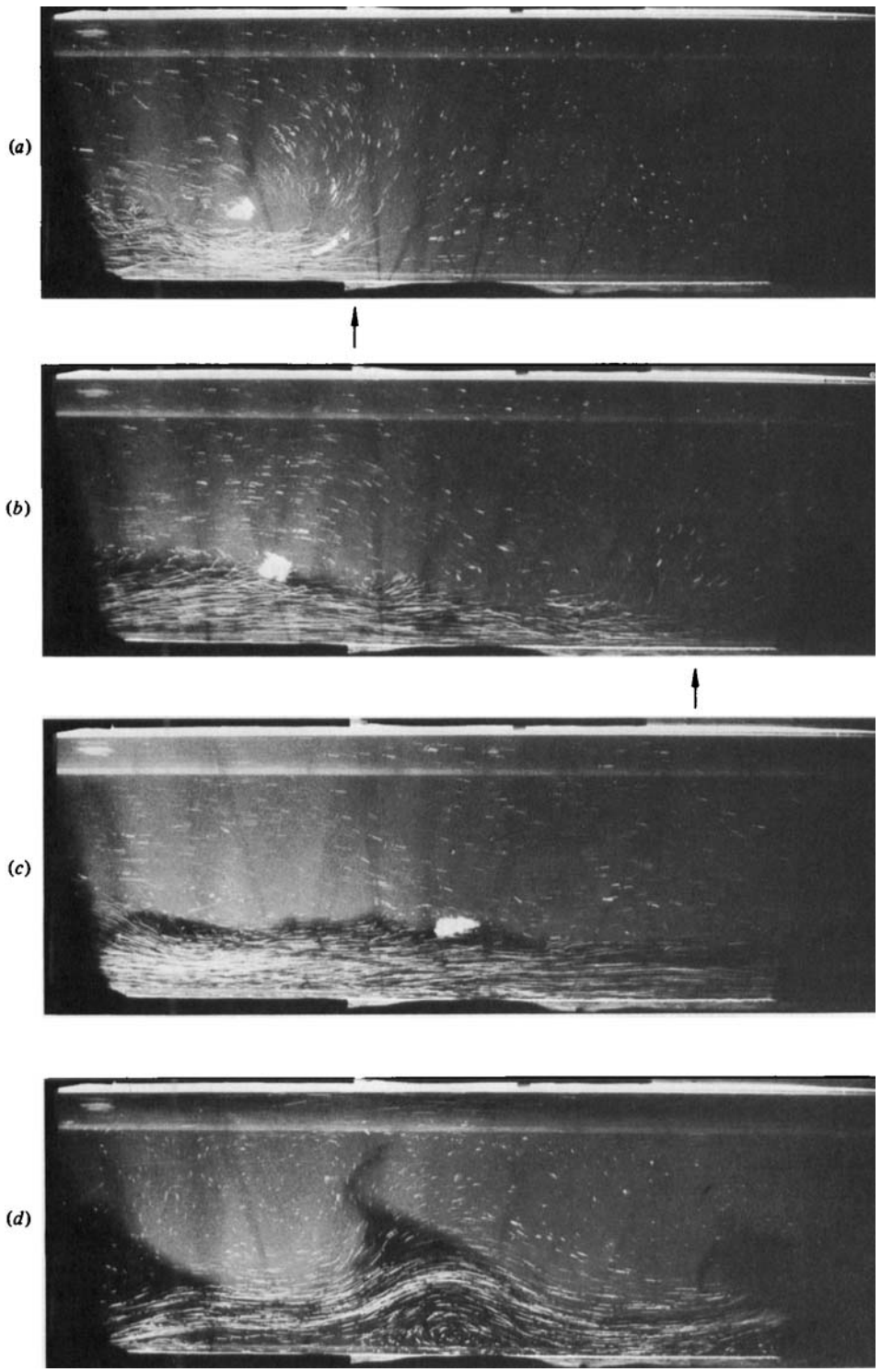
(a)
(b)
(c)
(d)

driven by inertial waves of very small frequency), while the first term on the right is the non-rotating drag force per unit mass, $F_0/\rho$.

In order to make a comparison between the magnitudes of the individual terms in (6) we first resort to empirical observations, which show that the exponential decay of the nose velocity $u_N$ never corresponds to a variation of $u_N$ greater than 3 % during the timescale $(h_N/g')^{\frac{1}{2}}$ characteristic of accelerations due to the buoyancy force. This timescale is simply $(h_N/g')^{\frac{1}{2}} \approx f^{-1}(h_N/l_N)^{\frac{1}{2}} \approx f^{-1}$, both in the laboratory and in nature. Hence, *so long as the rapid oscillations of the flow at the nose are assumed to be of negligibly small amplitude* and only the smoothed velocity considered, the time dependence in (6) is very small compared with the buoyancy term near the nose. Well behind the nose, on the other hand, the $x$-derivatives of depth (and velocity) become very small (if perturbations due to individual eddy structures are smoothed out) and the time dependence cannot be neglected. We therefore discuss the dynamics of the boundary current by dividing the flow into two regions: very close to the nose the flow is assumed to be quasi-steady (despite small-amplitude high-frequency variability), while further upstream the buoyancy force is neglected and the flow is allowed to be unsteady. The most difficult task is to evaluate the magnitude of the wave drag.

### 7.2. *Evaluation of drag forces*

In order to understand the evolution of gravity currents in the presence of rotation, it is necessary to estimate the flux of momentum into the lower layer. For this purpose it is useful to consider first the forces acting on isolated solid bodies moving through a rotating fluid in a plane perpendicular to the rotation axis. Taylor (1923) showed that the net force $G$ on a two-dimensional object about which the fluid motion should be in a plane perpendicular to the rotation axis is equal and opposite to the Coriolis force that would act on a mass of fluid with the same volume as the object. Thus the force is normal to the direction of motion and $G = \rho f u_* V$, where $\rho$ is the density of the fluid, $u_*$ the velocity of the object and $V$ its volume. For three-dimensional objects and finite Rossby numbers there is no longer such a simple result and the object experiences a force at some angle to the direction of motion.

By attaching solid bodies to a spinning disk or suspending them as the bob of a pendulum immersed in a rotating container of water, Mason (1975) was able to measure the steady forces on objects of various shapes. He found that, as the Rossby number $Ro = u_*/2\Omega l$ increased from $5 \times 10^{-3}$ to 0.5, the component $F_D$ of the force (per unit volume) in the direction opposite to the motion (the drag force) increased from a small value that was solely due to Ekman-layer friction up to the value $F_D = 0.5(G/V)\,l/a$, where $l$ is the width of the object and $a$ its length parallel to the direction of motion. This force also varied with the height $h$ of the body, the value quoted above being the maximum, which occurs at $h/(al)^{\frac{1}{2}} \approx 1$. On the other hand, the force acting normal to the direction of motion decreased from $G$ at $Ro < 10^{-2}$ to zero at the larger Rossby numbers. These forces further depend on the total depth

FIGURE 19. Time exposures of particles in both fluids in a horizontal sheet of light 1–3 cm below the surface and taken (*a*) 0.48, (*b*) 0.76, (*c*) 1.27 and (*d*) 7.9 rotation periods after opening of the lock. An arrow marks the nose position in (*a*) and (*b*) but it is 30 cm past the end of the viewing section in (*c*). The width of the channel (30 cm) serves as a scale. Frame (*d*) was taken at a very large time and shows the first rotationally dominated waves to grow on the upstream flow. Total exposure time 1.56 s (with direction indicated by a dot at the end of each streak line). Rotation is anticlockwise. Initial conditions are as in figure 18.

$D$ of the fluid, and Mason showed that the measurements for a given object shape collapse onto a single curve when plotted against the parameter $\mathscr{T} \equiv (2\Omega l/u_*)\,h/D$. This is the parameter that was first introduced by Hide (1961) and verified experimentally by Hide & Ibbetson (1966) as that which determines the presence or absence of a Taylor column above the solid body. For $\mathscr{T} > 100$ a Taylor column (extending throughout the depth of the fluid) is present, while for $\mathscr{T} < 1$ no column forms. Thus Mason's measurements indicate that the forces on moving bodies depend upon the presence or absence of a Taylor column. The drag force is given roughly by $F_D \approx 0.5\rho f u_*(l/a)$ for $\mathscr{T} < 4$, conditions under which no Taylor column exists.

The above results apply only at $Ro < 1$. The reason for this can be seen by considering the total drag $F_D$ as being the sum of a drag $F_\Omega$ that is due to the radiation of momentum by inertial waves and a 'non-rotating' drag $F_0$, which is simply the drag per unit volume $\frac{1}{2}C_D\rho lhu^2/V$ ($C_D$ a dimensionless drag coefficient) that would act in a non-rotating system. Thus the right-hand side of (6) is $(F_0+F_\Omega)/\rho = F_D/\rho$. In Mason's experiments with $Ro \leqslant 0.5$, $F_D$ was always much greater than $F_0$. However, the ratio of the two is proportional to the inverse of the Rossby number ($F_D/F_0 \approx \frac{1}{2}G/F_0 \approx C_D^{-1}Ro^{-1}\,(l/a)^{-1}$), and therefore the non-rotating drag should become dominant at large Rossby numbers if $l/a \approx 1$.

Returning attention to the gravity currents, we can consider the nose and each billow or eddy as moving obstacles that create inertial waves and Taylor columns in the lower layer, though the presence of the vertical wall and the flexibility of the shape of the density interface are additional complexities whose effects cannot be estimated at this stage. Very close to the nose the appropriate Rossby number $u_N/fl_N$ is rather large and, since $\mathscr{T} < 0.25$ whenever $h_N < \frac{1}{2}D$, no Taylor column exists (in either layer). Hence the total drag is likely to be dominated by the non-rotating contribution $F_0$ (though this conclusion depends on the value of the drag coefficient $C_D$) and the second term on the right of (6) will be small. Since we are assuming that the flow at the nose is quasi-steady, we are left with the inertial-buoyancy balance that applies at the nose of a non-rotating gravity current (Benjamin 1968). Some distance behind the nose, on the other hand, the upper layer is a turbulent flow, for which we are interested in the mean streamwise velocity $\bar{u}$. The mean cross-stream velocity vanishes, so that (6) is valid on all streamlines, not just that at $y = 0$. Since in this region we are neglecting the streamwise derivatives the wave drag cannot be neglected and we are left with a purely inertial motion which is driven by the momentum possessed by the fluid when it leaves the lock. Below we discuss the implications of the momentum balances in each region.

### 7.3. *Quasi-steady flow at the nose*

Since the nose velocity $u_N$ is only slowly varying in time it is possible to transform (6) to the frame of reference moving with the nose. The inertia–buoyancy balance appropriate at the nose then yields the Bernoulli invariant along the streamline on the wall:

$$\frac{\partial}{\partial x}[\tfrac{1}{2}(u-u_N)^2+g'h] = 0 \quad (y = 0). \tag{7}$$

Benjamin discussed the solution of (7) for two-dimensional non-rotating gravity currents (for which it applies at all values of $y$). By applying it on a streamline in each layer and passing through the stagnation point at the nose, he showed that the dynamic pressure at the nose is equal to that far behind the nose. Thus

$$\tfrac{1}{2}(u_u-u_N)^2+g'h_u = \tfrac{1}{2}u_N^2, \tag{8}$$

where $u_u$ and $h_u$ are the fluid velocity and depth far behind the nose. In this steady two-dimensional case the mass flux relative to the nose must be equal to any detrainment due to mixing across the density interface, but, if the mixing is neglected, $u_u = u_N$ and (8) gives $u_N = (2g'h_u)^{\frac{1}{2}}$. Laboratory experiments (Britter & Simpson 1978; Simpson & Britter 1979) show that mixing has a measurable effect, causing the upstream velocity to be greater than the nose velocity, and therefore, by (8), increasing the nose velocity.

For the three-dimensional gravity current in a rotating system, Stern *et al.* (1982) followed Benjamin's approach to obtain (8) for the streamline on the wall. In this case the presence of cross-stream fluid motions normal to the wall at the nose (as well as mixing) imply that a mass flux toward the nose is necessary at some values of $y$, and possibly at $y = 0$. Hence $u_u = u_N$ cannot be assumed. In order to solve (8) for the nose velocity (but again assuming no dissipation or vertical mixing), Stern *et al.* evaluated the upstream flow velocity $u_u$ on the wall by applying a similarity solution for a two-layer flow with uniform potential vorticity and no variation in the streamwise direction. This solution has a hyperbolic cross-stream velocity profile with a minimum at the wall.† The calculated nose velocity is almost independent of the potential vorticities and ratio of layer depths and lies in the range $1.54 < u_N/(g'h_u)^{\frac{1}{2}} < 1.57$. (The corresponding current widths lie in the range 0.41–0.52 deformation radii $(g'h_u)^{\frac{1}{2}}/f$.)

On the other hand, the observations reported in this paper, in particular the upstream velocity measurements, indicate that the similarity solution does not give a good description of the flow far behind the nose. We wish to stress that the measured wall velocity far upstream is *negative* relative to the nose, while the model predicts large positive values (e.g. $u_u - u_N = 2.18(g'h_u)^{\frac{1}{2}}$ for the case of zero potential vorticity). Furthermore, our observations of motions in the lower layer suggest that this discrepancy is most probably due to the transfer of a significant amount of energy into the lower layer and to turbulent dissipation upstream of the first large billow. (This is discussed further in §7.4.) A two-dimensionalization of the motions in both layers under the influence of the background rotation (as predicted by the Taylor–Proudman theorem) implies that the energy loss is experienced even by the streamlines that pass along the free surface. Thus an application of (7) beyond the laminar nose region is invalid and no reliable prediction of the nose velocity is possible in the absence of a more complex model for the flow. Intuitively, though, the nose velocity and the relative fluid velocity are still expected to scale, at least to some extent, with $(g'h_u)^{\frac{1}{2}}$, since this is the only characteristic velocity scale (other than that based on $H_0$) and since, to a first approximation, the buoyancy–inertia balance holds near the nose. Dissipation associated with turbulent mixing, as well as a small wave drag on the nose itself, are also expected to reduce the velocity below that predicted by Stern *et al.* The data on figures 11 and 12 show that $u_N \approx 1.3(g'h_u)^{\frac{1}{2}}$.

### 7.4. *Wave drag on the upstream flow and exponential decay*

With streamwise gradients neglected, integration across the current of the momentum balance yields

$$\int_0^l h\frac{\partial \bar{u}}{\partial t}\,\mathrm{d}y \approx -\frac{1}{\rho}\int_0^l h(F_0 + F_\Omega)\,\mathrm{d}y, \tag{9}$$

where $l$ and $h$ are the width and depth of the upper layer. The term on the right of

† This minimum velocity was predicted to be always positive relative to the nose, but then the streamlines on figure 3 of Stern *et al.* are inconsistent with their model, since they indicate a broad region of flow *away* from the nose *against* the wall (a negative velocity).

(9) is the total inertial drag per unit length and will be estimated from Mason's measurements of the forces on solid bodies.

The drag on the upper layer is associated with translational motion and other temporal variations of the billows and vortex structures, which tend to couple together the flow in the two layers. These structures are observed to move with a speed that is an order of magnitude less than the speed of the nose, but have dimensions comparable to the current width (a property that may or may not hold at geophysical scales, see §9.3), so that the corresponding Rossby number is of order $10^{-1}$ or less. On evaluating Hide's parameter $\mathscr{T}$ in each layer by using the current depth as a topographic height for the interface, we see that the eddy motions in the upper layer are two-dimensional and therefore tend to 'trap' much of the fluid moving along the current, while, for deep lower layers with $D/h_u > 10$, we find $\mathscr{T} < 1$. Thus vortex motions are not expected to reach the bottom and the results from solid bodies suggest that the drag is dominated by the effects of rotation ($F_0 \ll F_\Omega$). Neglecting the dynamically free shape of the density interface, we write the drag per unit length as

$$\int_0^l h F_\Omega \, \mathrm{d}y \approx k \rho f \bar{u} l h_u,$$

where the depth perturbations and horizontal dimensions of eddies are assumed to scale with $h_u$ and $l$ respectively. The introduced constant $k$ is expected to take values of the order of $10^{-1}$. With this, (9) becomes

$$\frac{\partial \bar{u}}{\partial t} \approx -kf\bar{u}, \tag{10}$$

which gives, after non-dimensionalizing by an absolute scale,

$$\frac{\bar{u}(x)}{(g'H_0)^{\frac{1}{2}}} \approx G(x)\, \mathrm{e}^{-kf(t-t_N)}, \tag{11}$$

where $t_N$ is the time at which the nose passes the position $x$. The function $G$ is by assumption slowly varying in $x$. It decreases with increasing distance along the wall because the velocity of the nose decreases, and is of order one if $\bar{u}$ is to be of order $(g'H_0)^{\frac{1}{2}}$ at the nose.

In this simple model for the flow, the 'rotating drag' in (10) is a force that is experienced by the fluid upstream but not directly by the nose itself. However, the dominance of the wave drag over the non-rotating drag $F_0 = \rho \bar{u} \partial \bar{u}/\partial x$ implies that (10), (11) describes the velocity of fluid parcels as well as the velocity at a fixed position $x$. The exponential decay upstream will therefore cause a net mass flux away from the nose, hence an exponential decay of the nose velocity. If the exponential decay time from (11) is compared with the empirical relations (3) and (4) for the decay time of the nose velocity, the empirical value of the coefficient $k(= \tau^{-1})$ is always in the range $0.01 < k < 0.1$. These values are a little smaller than expected and might be suppressed to some extent by the unsteady response of the lower layer near the beginning of each run. From Hide's parameter, a columnar mode (see also Heikes & Maxworthy 1982) in a steady flow will penetrate a distance $d \approx h(fl/u)$, but in the unsteady case it will require a time $d/c_g$ (where $c_g$ is the group velocity of low-frequency inertial waves) to be established. This time in our experiments is typically of the order of $20f^{-1}$, which in many runs is a large fraction of the observation time. This unsteadiness may also contribute to the scatter in the values of the decay time in figure 10.

| Run no. | $g'$ (cm s$^{-2}$) | $f$ (s$^{-1}$) | $\frac{H_0}{D}$ | $\overline{Re_N}$ | $E_0$ ($10^{-4}$) | $R_0$ (cm) | $\frac{A_0^{\frac{1}{2}}}{R_0}$ | $\tau$ | $\left(\frac{R_0}{A_0^{\frac{1}{2}}}\right)^{\frac{3}{2}}\tau$ | $\frac{x_M}{(R_0 A_0)^{\frac{1}{3}}}$ |
|---|---|---|---|---|---|---|---|---|---|---|
| 50 | 11.5 | 0.757 | 0.88 | 2600 | 1.7 | 13 | 1.85 | 102 | 68 | 54 |
| 51 | 11.0 | 0.251 | 0.86 | 1800 | 5.9 | 38 | 0.648 | 87 | 116 | 91 |
| 52 | 10.2 | 1.514 | 0.80 | 3200 | 1.0 | 6.0 | 4.11 | 208 | 81 | 62 |
| 53 | 9.4 | 0.881 | 0.87 | 1900 | 1.7 | 10.0 | 2.44 | 250 | 138 | 103 |

TABLE 1. Results from experiments in which the boundary current flowed onto a shallow lower layer ($D = 10$ cm). The mean nose Reynolds number $\overline{Re_N} = \overline{u_N h_n}/\nu$ and Ekman number $E_0 = \nu/fH_0^2$ are such that viscosity is not expected to affect the results. The exponential decay time $\tau$ and limiting distance $x_M$ have uncertainties of about 10%. $R_0 = (g'H_0)^{\frac{1}{2}}/f$ is the initial deformation radius, $A_0^{\frac{1}{2}}$ the lock dimension.

## 8. Intrusions over a shallow lower layer

Only flow over a deep lower layer has so far been considered. This is the simplest case because momentum is radiated away from the upper layer into an effectively semi-infinite fluid. If, on the other hand, the lower-layer depth $D$ is comparable to the depth of the current then the response of the lower layer to low-frequency forcing at the density interface will be different. For $h_u/D = \frac{1}{2}$, Hide's parameter takes values $\mathscr{T} \gtrsim 5$, which suggests that columnar structures in the lower layer may reach the bottom, as indeed would have the intense vortices on figure 19 had the lower layer been shallow. The consequent drag force on the upper layer will be smaller than that exerted in the case of a deep lower layer as the whole of the fluid beneath the current, being trapped in a series of Taylor columns, will tend to move with the upper layer and thereby reduce relative motion.

In order to test the importance of the lower-layer depth and the rotating-drag hypothesis, a number of experiments were carried out with a shallow lower layer. All conditions were similar to those outlined in §2, except that $D = 10$ cm and only lock A was used. The fresh water in the lock occupied 80–90% of the total fluid depth, and the depth of the nose near the beginning of each run was close to $\frac{1}{2}D$. The upper-layer flow appeared to be qualitatively the same as that observed with a deep lower layer, though rotationally dominated (quasi-geostrophic) waves this time became visible on the current just outside the lock after only four to five rotation periods, about the time at which the nose reached the far end of the channel. The nose velocity again decreased with time in a manner that was well described by an exponential law of the form (3). The decay timescale $\tau$ obtained by applying (1) and (3) is given in table 1, along with other parameters of the system. All of the values of $\tau$ are three to five times greater than those expected with a deep lower layer (figures 9 and 10), but show a very similar dependence on the Froude number $Fr = A_0^{\frac{1}{2}}/R_0$. Hence the results support the prediction that less momentum is transferred to a shallow lower layer, leading to a slower exponential decay of the nose velocity.

## 9. Conclusions and further discussion

### 9.1. *Summary of the results*

The release of a volume of buoyant fluid from a lock at one end of the long rotating channel gives rise to a three-dimensional gravity current that propagates along one wall of the channel and a Kelvin wave that propagates around the lock. At the high Reynolds numbers achieved, the gravity current flow is turbulent and some of the

general features of the rather complex flow are sketched on figure 16. As in the case of a non-rotating two-dimensional gravity current, billows grow beneath the current a short distance behind the leading edge of the nose, dissipating energy and causing mixing between the two fluids. There appears to be no permanent and stable flow near the nose, since new billows periodically appear, break up the head of the current and cause rapid oscillations of the nose velocity. For large Reynolds numbers the billow dimensions and growth times are identical to those measured for currents in a nonrotating system, with billow frequencies as large as 20 times the rotation frequency $\Omega/2\pi$ being measured in some runs. We conclude that the instability is of the Kelvin–Helmholtz type and is little influenced by the background rotation, though of course the width of the basic flow at the nose remains strongly controlled by rotation. The resulting three-dimensional turbulence is characterized initially by large Rossby numbers (the dominate length scaling with current depth) but decays with distance behind the nose as billows are left behind on the training current. Eddies with larger scales reach small Rossby numbers and become strongly influenced by the background rotation, which causes more rapid dissipation of the horizontal components of vorticity and a corresponding two-dimensionalization of the flow field. The predominantly horizontal eddy motions may therefore scale with the current width, which is the largest scale present, but we cannot be certain of this as the laboratory experiments were necessarily conducted with comparable current depths and widths. The upstream eddies are found to be accompanied by cyclonic vortices that penetrate many current depths into the lower layer near the sidewall. Vertical mixing across the density interface also appears to be more vigorous than in the non-rotating case and is probably assisted by vertical (axial) flow within the vortices in the lower layer (see §9.2).

The billows and eddies in the boundary current also cause horizontal spreading of the buoyant fluid away from the wall. However, this spreading is opposed by Coriolis forces associated with the mean streamwise velocity of the eddies. Measurements of the velocity profiles upstream and concomitant measurements of the total width of the dyed upper-layer fluid indicate that the outer edge of the dye is the best definition of the upstream width. This width increases significantly with distance behind the nose, from 0.6 *local* deformation radii at the head to approximately one *initial* deformation radius $R_0 = (g'H_0)^{\frac{1}{2}}/f$ at a distance $10R_0$ upstream. This suggests that Stern's (1980) limiting bore solution is realized near the nose, while other factors associated with the turbulent two-layer flow broaden the upstream flow.

Measurements of the position of the nose as a function of time show that, after a short initial period of acceleration, the nose velocity $u_N$ decreases with time in a way that in every run is well described by an exponential (after smoothing the small-amplitude oscillations). In some cases the velocity falls to less than 20% of its initial value before the nose reaches the end of the channel. Though the depth of the current could not be measured as accurately, it too decreases with time and the local Reynolds number sometimes becomes so small that complete stagnation is avoided by an adjustment to the viscous motion of a thin wedge. When dissipation due to Ekman friction is small, the dimensional timescale $\tau/f$ for the decay of the nose velocity depends only upon the rotation rate $\Omega$ and a Froude number $Fr = fA_0^{\frac{1}{2}}/(g'H_0)^{\frac{1}{2}}$ that describes the flow leaving the lock. Thus with a deep lower layer ($D/h \gtrsim 10$) we find $\tau \approx 25Fr^2$ and the corresponding distance to which the nose could travel at $t \to \infty$ is $x_M \approx 22(R_0 A_0)^{\frac{1}{2}}$. An additional dependence upon the Ekman number occurs when $\nu/fH_0^2 > 10^{-3}$, as the vorticity of the mean flow is then dissipated by Ekman boundary layers.

We have proposed a theoretical model for the flow in which the propagation of the nose is governed by the same inertia–buoyancy balance that determines the speed of the nose of a gravity current in a nonrotating system. In the rotating case, however, an exponential decay of the flow results from the transfer of momentum to the lower layer by inertial waves and associated columnar vortices. These exert a total drag on the upstream flow that scales with the Coriolis force $f\bar{u}$, where $\bar{u}$ is a mean downstream velocity. Vortices and wave motions in the deep lower layer were observed and a predicted increase of the decay time with decreasing depth of the lower layer was verified by experiments with intrusions over a shallow fluid. However, further work is needed to quantify the dependence upon fluid depth. The influence of mixing across the density interface has not been taken into account as density differences for these experiments were necessarily small and measurement of further dilutions as the current propagates down the channel were impossible.

The possible implications of the exponential decay for ocean currents are best demonstrated by a simple example. A 'small' deformation radius $R_0 \approx 10$ km and a small horizontal dimension of just $A_0^{\frac{1}{2}} \approx 10^2$ km lead to a limiting travel distance $x_M \approx 10^3$ km (from (4)), and we therefore expect only small variations of velocity for intermittent currents of the scale of large naturally occurring boundary currents before they cross an ocean basin or are strongly influenced by surface heat transfer, large-scale circulations and the variation of the Coriolis parameter. Nevertheless, as discussed below, such intermittent boundary currents will induce waves, vortices and a mean motion in the environmental fluid. Furthermore, the mean flow close to the nose will also be ageostrophic and this implies that calculations of geostrophic velocities from observed isopycnal slopes will overestimate the mass flux.

### 9.2. *Turbulence structure and its coupling with the lower layer*

The structure of the two-layer flow and the origin of the observed cyclonic vortices at the wall in the lower layer can be viewed in terms of the transition from three-dimensional to quasi-two-dimensional turbulence in a rotating system. Experiments with the production of turbulence by an oscillating grid in a rotating container (Dickinson & Long 1983; Hopfinger, Browand & Gagne 1982; Hopfinger, Griffiths & Mory 1983) indicate that a sharp transition occurs between a region of three-dimensional turbulence near the grid and a deep region of rotationally dominated and quasi-two-dimensional turbulence further away from the energy source. Transition is characterized by a local Rossby number $u'/l'f \approx 0.2$, where $u'$ and $l'$ are the local turbulence velocity and lengthscale respectively. This Rossby-number criterion corresponds to a forcing frequency $u'/l'$ (by three-dimensional eddies) for which inertial wave group velocities are predominantly in the direction of the rotation axis. It is also found that vortices aligned with the rotation axis and extending throughout the fluid depth $D$ form in a time of order $D(\Omega l)^{-1}$ after the grid is started from rest. This is just the travel time for low-frequency inertial waves. If forcing is neither too strong nor too weak for a given rotation rate $\Omega$, the cyclonic vorticity becomes concentrated into very intense cyclones whose relative vorticity can exceed $\Omega$ by one to two orders of magnitude (Hopfinger *et al.* 1982).

Returning now to the gravity current, it is plausible that relatively intense cyclonic vortices are generated in the lower layer by the turbulent field in the current. The observed small cyclonic vortices near the wall (figure 18*c*) seem to support this conjecture. Very close to the nose a local Rossby number based on a turbulent eddy velocity $u' \approx 0.3u_N$ and lengthscale $l' < h_u$ is much greater than 0.2. However, some distance behind the nose the turbulent velocity decreases to say $u' < 0.1u_N$, so that

scales of $l' \approx l_N$ give a Rossby number $u'/l'f < 0.2$. Turbulent eddies of this scale (and perhaps smaller) will therefore degenerate into vertical columnar (anticyclonic) structures which penetrate at the inertial wave speed deep into the lower layer (see for instance figures 2(*d*) and 3). These anticyclonic structures contain diverging flow and should therefore be rather diffuse as in the oscillating-grid experiments. However, between the anticyclones and near the wall there may be regions of converging flow, and hence vorticity concentration. The cyclonic vortices in our experiments first reach the observation depth (about 8 cm below the interface) at a distance of about 40 cm (or five head widths) upstream of the nose. This corresponds to a propagation speed for the columnar structures which is consistent with the inertial wave speed $l_N \Omega$. Thus, while billows tend to lead directly to visible cyclonic eddies in the upper layer at the outer edge of the flow, vorticity concentration may play a role in producing cyclones in the lower layer near the wall. Further work is needed to verify this hypothesis and to establish the horizontal scale of the vortices in terms of the current depth and width.

### 9.3. *The appearance of baroclinic waves*

Measurements reported in this paper were taken only at times before rotationally dominated waves had grown to visible amplitudes at any point on the current. Such waves grow first on the current just outside the lock and are similar to the *baroclinic* waves studied by Griffiths & Linden (1981, 1982) in experiments with uniform axisymmetric boundary currents. Unlike the Kelvin–Helmholtz billows near the nose of the intrusion, these waves break the constraint of rotation, and at large amplitude cause a large horizontal spreading of the buoyant fluid. However, they require times of the order of 10 rotation periods ($t > 10^2 f^{-1}$) to grow to a visible amplitude. In this time the nose of the current is able to travel a very large distance given by (2), or more readily by $x \approx 10^2 f^{-1}(g' H_0)^{\frac{1}{2}} \approx 10^2 R_0$. Moreover, the exponential decay of the flow makes it unlikely that the influence of the large-amplitude waves can overtake the nose before it approaches stagnation. In the slowly evolving stage near stagnation, however, the waves do have time to grow along the entire length of the flow. This can be seen occurring in experiments with slow continuous point sources of buoyant fluid (Stern 1980; Griffiths & Linden 1981), where the low-Reynolds number flow develops rotationally dominated instabilities close to the nose. We conclude that rotationally dominated instabilities do not affect high-Reynolds-number flow in transient gravity currents for a very large distance behind the nose.

This work was supported by the Centre National d'Exploitation des Océans under contract no. 82/2653 and carried out at the Institut de Mécanique de Grenoble.

## REFERENCES

BENJAMIN, T. B. 1968 Gravity currents and related phenomena. *J. Fluid Mech.* **31**, 209–248.

BRITTER, R. E. & SIMPSON, J. E. 1978 Experiments on the dynamics of a gravity current head. *J. Fluid Mech.* **88**, 223–240.

CHANDRASEKHAR, S. 1961 *Hydrodynamic and Hydromagnetic Stability.* Clarendon.

DICKINSON, S. C. & LONG, R. R. 1983 Oscillating-grid turbulence including effects of rotation. *J. Fluid Mech.* **126**, 315–334.

GILL, A. E. 1976 Adjustment under gravity in a rotating channel. *J. Fluid Mech.* **77**, 603–621.

GRIFFITHS, R. W. & LINDEN, P. F. 1981 The stability of buoyancy driven coastal currents. *Dyn. Atmos. Oceans* **5**, 281–306.

GRIFFITHS, R. W. & LINDEN, P. F. 1982 Laboratory experiments on fronts. Part I: Density-driven boundary currents. *Geophys. Astrophys. Fluid Dyn.* **19**, 159–187.

HEIKES, K. E. & MAXWORTHY, T. 1982 Observations of inertial waves in a homogeneous rotating fluid. *J. Fluid Mech.* **125**, 319–346.

HIDE, R. 1961 Origin of Jupiter's Great Red Spot. *Nature* **190**, 213–218.

HIDE, R. & IBBETSON, A. 1966 An experimental study of 'Taylor columns'. *Icarus* **5**, 279–290.

HOPFINGER, E. J., BROWAND, F. K. & GAGNE, Y. 1982 Turbulence and waves in a rotating tank. *J. Fluid Mech.* **125**, 505–534.

HOPFINGER, E. J., GRIFFITHS, R. W. & MORY, M. 1983 The structure of turbulence in homogeneous and stratified rotating fluids. *J. Méc. Théor. Appl. Suppl.* (to appear).

HUPPERT, H. E. 1968 On Kelvin–Helmholtz instability in a rotating fluid. *J. Fluid Mech.* **33**, 353–359.

KILLWORTH, P. D. & STERN, M. E. 1982 Instabilities on density-driven boundary currents and fronts. *Geophys. Astrophys. Fluid Dyn.* **22**, 1–28.

MASON, P. J. 1975 Forces on bodies moving transversely through a rotating fluid. *J. Fluid Mech.* **71**, 577–599.

ROTTMAN, J. W. & SIMPSON, J. E. 1983 Gravity currents produced by instantaneous releases of heavy fluid in a rectangular channel. *J. Fluid Mech.* **135**, 95–110.

SIMPSON, J. E. 1982 Gravity currents in the laboratory, atmosphere, and ocean. *Ann. Rev. Fluid Mech.* **14**, 213–234.

SIMPSON, J. E. & BRITTER, R. E. 1979 The dynamics of the head of a gravity current advancing over a horizontal surface. *J. Fluid Mech.* **94**, 477–495.

STERN, M. E. 1980 Geostrophic fronts, bores, breaking and blocking waves. *J. Fluid Mech.* **99**, 687–704.

STERN, M. E., WHITEHEAD, J. A. & HUA, B.-L. 1982 The intrusion of a density current along the coast of a rotating fluid. *J. Fluid Mech.* **123**, 237–266.

TAYLOR, G. I. 1923 Experiments of the motion of solid bodies in rotating fluids. *Proc. R. Soc. Lond.* **A104**, 213–218.

WADHAMS, P., GILL, A. E. & LINDEN, P. F. 1979 Transects by submarine of the East Greenland Polar Front. *Deep-Sea Res.* **26A**, 1311–1327.